Lab on a Chip

Devices and applications at the micro- and nanoscale

Accepted Manuscript

This article can be cited before page numbers have been issued, to do this please use: N. Singh, M. A. Ali, P. Rai, I. Ghori, A. Sharma, B. D. Malhotra and R. John, *Lab Chip*, 2020, DOI: 10.1039/C9LC00751B.

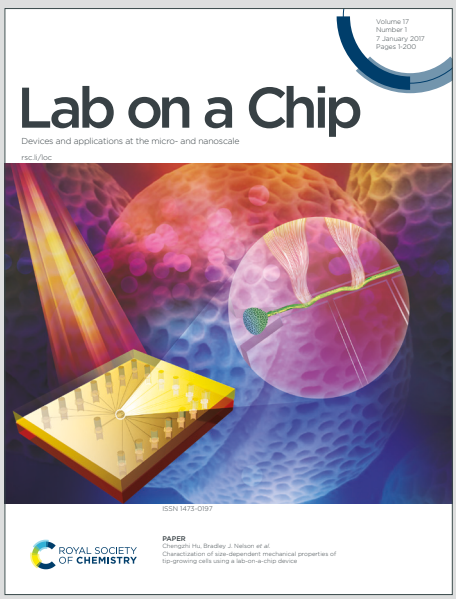

ROYAL SOCIETY OF CHEMISTRY

rsc.li/loc

View Article Online
DOI: 10.1039/C9LC00751B

Dual-modality microfluidic biosensor based on nanoengineered mesoporous graphene hydrogels

Nawab Singh[a], Md. Azahar Ali[b], Prabhakar Rai[c], Inayathullah Ghori[a,d], Ashutosh Sharma[c], B. D. Malhotra[e]*, and Renu John[a]*

[a]Department of Biomedical Engineering, Indian Institute of Technology Hyderabad, 502285 Telangana, India.
[b]Department of Aerospace and Mechanical Engineering, University of Notre Dame, Notre Dame, Indiana- 46556, USA.
[c]Department of Chemical Engineering, Indian Institute of Technology Kanpur, Kanpur, 208016, India.
[d]Department of Cardiology, Kamineni Koti Hospital, Hyderabad-500001, Telangana, India.
[e]Department of Biotechnology, Delhi Technological University, Shahbad Daulatpur, Main Bawana Road, Delhi-110042, India.

Abstract

A dual-modality microfluidic biosensor is fabricated using mesoporous nanostructured cysteine-graphene hydrogel for the quantification of human cardiac myoglobin (cMb). In this device, nanoengineered mesoporous L-cysteine-graphene (Cys-RGO) hydrogel performs the role of a dual-modality sensing electrode for the measurements conducted using differential pulse voltammetry and surface plasmon resonance (SPR) techniques. High surface reactivity, mesoporous structure and fast electron transfer combined with good reaction kinetics of graphene hydrogel in this device indicate excellent performance for detection of human cardiac myoglobin in serum samples. In electrochemical modality, this microfluidic chip exhibits a high sensitivity of 196.66 μA ng mL^{-1} cm^{-2} for a linear range of concentration (0.004−1000 ng mL^{-1}) with low limit of detection (LOD) of 4 pg mL^{-1} while the SPR technique shows LOD as 10 pg mL^{-1} for cMb monitoring in the range, 0.01−1000 ng mL^{-1}. The intra-assay coefficient of variation was less than 8% for standard samples and 9% for real serum samples, respectively. This Cys-RGO hydrogel-based microfluidic SPR chip allows real-time dynamic tracking of cMb molecules with a high association constant of $4.93 \pm 0.2 \times 10^5$ M^{-1} s^{-1} and a dissociation constant of $1.37 \pm 0.08 \times 10^{-4}$ s^{-1}, self-verification, reduced false readout, and improved detection reliability.

Keywords: Dual-Modality, Microfluidic device; Cysteine-Graphene Hydrogel; Cardiac Myoglobin; Electrochemical; Surface plasmon resonance

***Corresponding authors:** renujohn@iith.ac.in*, Ph: +91-40-23016097, bansi.malhotra@gmail.com*

DOI: 10.1039/C9LC00751B

1. Introduction

Nanostructured hydrogels have become increasingly popular as electrochemical transducer materials for biomedical sensors owing to inherent properties of electron transfer ability, facile functional versatility, biocompatibility, stability, biological scaffolds and hydrophilicity towards aqueous microenvironments. Different hydrogels including chitosan, silk fibroin, poly-N-isopropylacrylamide and nanostructured cellulose have been exploited to fabricate biosensors due to their un-precedented mechanical strength, chemical inertness, electrical conducting properties, easy to encapsulate with cells, drugs, enzymes and abundant functional groups[1]. Graphene has been utilized as an excellent hydrogel material to realize signal transduction for biosensors and bioelectronic devices[2] and development of innovative biomaterials. Graphene oxide nanocomposite hydrogels were used as near-infrared light-driven valves[3] and opal hydrogel particles were used as facile pesticides monitoring[4]. With multiple functional moieties, graphene–hydrogel hybrid nanocomposite has been used to encapsulate alcohol oxidase for monitoring of methanol concentration via catalytic reaction on the sensor surface[5]. This hydrogen-based nanosensor showed a high sensitivity, low limit-of-detection (LOD), and rapid detection due to nano formation of graphene-hydrogel.

With exciting electronic, electrochemical properties and high functionality with high surface area, the reduced graphene oxide (RGO) was used both for the development of nanoelectronic transistors and optofluidic biosensing devices[6–11]. Specifically, RGO was utilized for detection of influenza virus, H1N1[11], cancer biomarkers[12] and D-amino acid enantiomer[13] due to porous surface and tuning of electrical conducting properties. The presence of functional groups resulted in improved immobilization of biomolecules (antibodies, enzymes, peptides DNA etc.)[8,14]. In RGO, oxygen bonded to carbon atoms with 25% sp^3 hybridization perhaps enabled covalent conjugation with biomolecules. The hexagonal carbon structure, crystalline nature and occurrence of defects and functional groups in RGO lattice are known to affect electrical properties such as electrochemical reactivity, mass transfer of electrons and surface adsorption owing to increased sp^2 bonds that may have enhanced sensitivity and reaction time of biosensor[9,10,15]. However, the attachment of RGO in solution formed on gold surface was found to be unstable due to its weak binding affinity with gold surface. Thus, the modified RGO with a self-assembled monolayer of L-cysteine amino acid (Cys) is an alternative approach for the development of electrochemical or surface plasmonic biosensor. Cys has been reported to enable stable thin film formation on gold surface by imparting thiol (-SH) groups that may allow covalent bond formation with gold. Nanocomposite of hydrogel of Cys and RGO could provide an interesting substrate with abundant carboxylic groups that may result in increased loading of the antibody molecules, high surface absorption ability and good stability resulting in enhanced sensitivity of target

View Article Online
DOI: 10.1039/C9LC00751B

molecules[16,17]. In addition, Cys-RGO hydrogel can be an excellent material for the development of surface plasmonic resonance based biosensors and electrical transducers in microfluidic devices.

Integration of functional Cys-RGO hydrogel with a microfluidic device may result in improved point-of-care (POC) detection performance of a target molecule. Microfluidic structures have been found to provide several benefits including miniaturization, improved portability and reduced analysis time with low sample volume[18–21]. Direct integration of nanostructures with microfluidic devices has been explored in numerous reports for the development of POC biosensors[22–24]. For example, nanostructures of zinc oxide, boron-doped diamond, nickel vanadate hollow-nanospheres and zinc oxide nanowires were combined with microfluidic devices for quantification of circulating tumour cells in blood[25], pesticide atrazine[26], cardiac troponin I[27] and glucose[28]. Application of Cys-RGO hydrogels for the development of multi-microfluidic biosensors is an interesting application that has as yet not been explored.

Quantification with multiple sensing modalities from a single sensor has been found to enhance detection reliability and decrease false readouts. Ali *et al,* have demonstrated a three-dimensional plasmonic nanopost-array-based microfluidic platform to realize dual-modality sensing capability of breast cancer biomarker with femtomolar sensitivity[29]. It has been shown that the integration of dual modalities on same sensing surface in a microfluidic device decreases the sample volume required for both sensing modalities. The electrochemical sensing platform offers potential merits including high sensitivity due to high signal-to-noise ratios, low limit-of-detections (LOD), and short response time. The SPR-based diagnostics provides a promising platform owing to multiplexing, dynamic tracking of biomolecules, kinetic analysis and high specificity[17]. Singh *et al.* have reported a surface plasmon resonance (SPR) immunosensor for anti-cholera toxin monitoring based on non-covalently functionalized monolayer graphene[30]. Primo *et al.* have demonstrated graphene oxide-based immunosensor for the quantification of galectin-3 using SPR method[31]. In this work, we report the development of a dual-modality microfluidic biosensor using Cys-RGO hydrogel incorporating the electrochemical and SPR modalities to reduce false signal and self-verification for the monitoring of acute myocardial infarction (AMI) in real serum samples.

Cardiac vascular diseases (CVDs) are known to be a major threat to humans[32,33]. According to the World Health Organization (WHO), an estimated 17.9 million (31%) people die every year from CVDs of all worldwide deaths in 2015[34,35]. AMI or heart attack is related to the coronary heart artery disease that occurs due to progression of atherosclerotic plaques inside the coronary heart blood vessel endothelium. Cardiac biomarkers such as myoglobin (cMb), creatine kinase (CK-MB), and cardiac troponins T and I monitoring is essential for early screening and diagnosis of AMI. cMb is one of the earliest biomarkers released in blood serum by the myocardial cells following a myocardial

damage[36]. Several label-based methods have been reported for cardiac biomarker detection including radio immunoassays[37], chemiluminescent immunoassays[38] and enzyme-linked immunosorbent assays[39,40]. These conventional assays have several drawbacks such as the need for several processing steps, long durations for detection and poor sensitivity[41]. This work explores the development of a dual-modality microfluidic sensing platform on a chip using Cys-RGO hydrogel with mesoporous and biocompatibility features that can offer low LOD, high accuracy, high-sensitivity and high binding kinetics for monitoring of cardiac myoglobin.

We report a dual-modality microfluidic sensor using Cys-RGO hydrogel for quantification of cardiac myoglobin. A patterned gold (Au) was first modified with of Cys-RGO hydrogel and then *in-situ* functionalized with specific antibodies of cardiac myoglobin via EDC-NHS chemistry (Fig. 1) followed by integration on a PDMS microchannel. The dual-modality performance using SPR and differential pulse voltammetry methods was carried out to quantify the cardiac myoglobin biomarker and real-time binding kinetic analysis. In our findings, the electrochemical sensing modality showed a high sensitivity of 196.66 μA ng mL^{-1} cm^{-2} with a low LOD of 4 pg mL^{-1}. However, the SPR sensing modality showed an LOD of 10 pg mL^{-1} for cMb sensing. The graphene-hydrogel in electrochemical mode exhibited increased sensitivity, high reproducibility and high stability due to porous structure of the hydrogel. The sensor could be utilized to measure myoglobin in real serum sample in the concentration range, 0.04–500 ng mL^{-1}. In this SPR-chip, the observed high association constant of antibody-antigen interactions indicated high affinity and good selectivity of target biomarkers.

2. Experimental section

2.1 Device fabrication

The microfluidic device was fabricated via soft lithographic method (Fig. 2). For counter and working electrodes, gold/glass plate of thickness (100 nm) was patterned using gold (Au) etchant having dimension of 3mm × 2cm while for reference electrode, a 500 nm thickness of silver (Ag) layer was deposited on glass plate using direct current (DC) sputtering by placing a shadow mask. Further, the Ag electrode was treated with 0.1 M KCl solution for 60 s to obtain silver-silver chloride (Ag-AgCl) layer. For Cys-RGO hydrogel formation, RGO was synthesized using well-established Hummer's method with a modification[21]. In brief, 10 mg of RGO was dispersed in 50 mL DI water with sonication for 3 h at 60 °C and the dispersed solution was kept overnight at magnetic stirring condition (600 rpm) at 80 °C. This aqueous colloidal solution was centrifuged at 15000 rpm for 30 min, was dried and then 50 mL of thionyl chloride ($SOCl_2$) solution, was added. This solution ($SOCl_2$+RGO) was refluxed using magnetic stirring for 24 h after which it was centrifuged followed by washing with THF after which it was dried under vacuum. Next, $SOCl_2$ modified RGO was added into 100 mM aqueous solution of L-cysteine via

View Article Online
DOI: 10.1039/C9LC00751B

magnetic stirring at 37 °C for 12 h and NaOH solution was used to adjust pH at 8.5. Then centrifuged at 15000 rpm for 30 min and was then freeze dried. This step led to the substitution of the acyl group (−COCl) with −CO−NH amide group on the edges of RGO. The NH_2 group of Cys was used to form the amide bond with the RGO's COOH group whereas other functional groups were free on the RGO surface[42]. The functionalization of (COOH)(CH_2SH)−CH−RGO was accomplished with a significant amount of (−COOH) functional groups for covalent bonding with antibodies by introducing amide bond formation. The proposed mechanism regarding the formation of Cys-RGO hydrogel nanostructure is shown in Fig. 1.

After formation of the Cys-RGO hydrogel, one of the Au electrodes was treated with Cys-RGO hydrogel solution by dipping the entire substrate into the solution for 12 h whereas the other electrodes were protected with the shadow mask. A coating of self-assembled monolayer of Cys-RGO hydrogel was formed on the Au surface due to presence of thiol groups (−SH) which facilitated the formation of covalent bond of Au−S. Separately, a microfluidic channel of dimension (height and width, 200 µM) was fabricated and bonded with glass containing Au, Cys-RGO hydrogel and Ag/AgCl electrodes via oxygen plasma treatment (Fig. 2 and 3).

For immunoassay of cMb monitoring, the antibody-antigen based interaction was employed in this microfluidic sensor. To immobilize the cMb antibodies EDC-NHS coupling chemistry was used to activate the −COOH groups of Cys-RGO/Au hydrogel-based electrode surface. The microfluidic device was kept at room temperature (25 ^oC) for 2 h and washed with PBS. The antibody (cMAb) solution (2 mg/mL) was injected via inlet of the microfluidic channel for the immobilization of cMAb. The carboxylic −COOH functional groups present on the Cys-RGO surface were conjugated with amine (−NH_2) groups of the cMAb via covalent interactions. Further, the antibodies immobilized Cys-RGO/Au electrode was treated with BSA solution to block the non-specific sites. After fabrication, the microfluidic immunoassay chip was stored at 4 ^oC for testing. A detailed note on the chip fabrication is provided in the Supplementary Information.

The immobilized cMAb on the sensor surface captured the cMb molecules directly via site-specific paratope and epitope interactions when cMb molecules were injected through the microfluidic device. This resulted in the formation of antigen-antibody immunocomplex on sensor surface. The recognition event on the sensor electrode surface of antigen-antibody immunocomplex formation resulted in the change in signal that was detected using dual-modality transduction such as electrochemical and surface plasmonic techniques.

All experiments with serum samples were performed in accordance with the guidelines and protocols of the Kamineni Hospital, LB Nagar, Hyderabad, India and approved by the ethics committee

View Article Online
DOI: 10.1039/C9LC00751B

Kamineni Hospital, LB Nagar, Hyderabad, India. The participants were completely informed about the purpose of the study and consent was obtained.

2.2 Detection principles

The dual-modality microfluidic sensor is based on the principle of electrochemical differential pulse voltammetry (DPV) and optical SPR spectroscopy. In the DPV mode, a three-electrode based electrochemical microfluidic setup was used to detect electrode current using a potentiostat. This microfluidic sensor consisted of the reference electrode (RE), counter electrode (CE) and working electrode (WE) connected to electrochemical potentiostat to complete the electrochemical cell circuit. In principle, DPV is a derivative of linear sweep voltammetry having a series of regular small pulses that are superimposed on the potential linear sweep. The generated current was measured prior to each potential change and the current difference was plotted against potential. During DPV measurement, a fixed potential (–0.2 to 0.7 V) was maintained between the WE and RE (Ag/AgCl). The current generated was monitored between the WE and the counter electrode (CE). At WE, one of the half-cell of reactions within the electrochemical cell was controlled to investigate the change in charge transfer at the interface, the other half-cell reaction occurred at the CE[43,44].

For SPR measurements, the specific cMAb on electrode surface was first immobilized. The target molecules when flown on the surface of Au, result in the cMAb binding via affinity interaction, which subsequently induced enhancement in the refractive index (RI) at the sensor (SPR) surface. In the SPR analysis, response unit (RU) is employed to define the signal shift, where 1 RU is equivalent to a critical angle shift of 10^{-4} degree or 10^{-12} g mm^{-2}. In the beginning of the experiment when cMAb-cMb target interactions did not occur, the value of RU can be related to the initial critical angle. The change in refractive index, Δn_d, occurs within the layer of thickness (h) and is given as

$$\Delta n_d = \left(dn/dc\right)_{vol} \Delta\Gamma/h \qquad (1)$$

where $(dn/dc)_{vol}$ represents the increase in RI within the volume of analyte concentration c, and $\Delta\Gamma$ represents the target concentration (bound)[45,46]. The association rate constant (k_a) and dissociation rate constant (k_d) can be calculated using the binding kinetics equation[17].

$$A_{surface} + B \Leftrightarrow AB \qquad (2)$$

K_a and K_d constants are calculated as-

$$\frac{dAB}{dt} = K_a\,[A][B] \qquad (3)$$

View Article Online
DOI: 10.1039/C9LC00751B

$$\frac{dAB}{dt} = K_d\,[AB] \quad (4)$$

Equilibrium rate constant from equation (3) and (4) as-

$$K_d\,[AB] = K_a\,[A][B]$$

$$\frac{K_d}{K_a} = \frac{[A][B]}{[AB]} = K_D$$

The parameter related to RI of the medium can be utilized to detect the desired antigen that binds with the specific antibodies on the sensor surface. In the SPR detection mode, the LOD depends on the SPR sensing performance of the sensor, immobilized surface coverage of the antibodies and binding affinity[46].

The cMAb–cMb interaction was determined by the SPR measurement conducted at 25 °C. In the SPR measurement, the non-linear curve fit was achieved to calculate the association phase during binding via a software that was used for kinetics evaluation. On attachment of the target molecule at the sensor surface, response can be evaluated via equation (2).

The rate of affinity of target molecule in association phase is given as follows

$$\frac{d[AB]}{dt} = K_a[A][B] - K_d[AB] \quad (5)$$

For the biomolecule interaction, the integrated rate equation in association phase is given by

$$R_t = \frac{K_a C R_{max}}{K_a C + K_d}(1 - e^{-(K_a[C] + K_d)t}) + R_0 \quad (6)$$

or $$R_t = E(1 - e^{-K_s t}) + R_0 \quad (7)$$

In the above equations, R_0 is the SPR signal at time 0. [C] is the target concentration and $E=K_aCR_{max}/K_aC+K_d$ is the shift. The related kinetic statistics can be found using $K_s=K_aC+K_d$. K_a and K_d were calculated from the plot between K_s and C (concentration of cMb) where slope provides K_a and y- intercept values and K_d.

3. Results and discussion

3.1 X-ray diffraction (XRD) studies

To confirm the crystalline nature of the synthesized RGO, we conducted the XRD analysis (Fig. 4a). A wide peak found at 2θ = 23.86 was related to (002) plane due to graphitic nature of RGO. An interlayer space of RGO was calculated as 1.76 nm by full-width at half maximum (fwhm) of 23.86 for (002) plane by Eq. 8.

View Article Online
DOI: 10.1039/C9LC00751B

$$d_{002} = 0.9\lambda/\beta_{002} \cos \theta_{002} \quad (8)$$

where d_{002} represents the distance between two graphene sheets and β_{002} represents fwhm.

3.2 Raman studies

The qualitative composition of Cys-RGO hydrogel was determined by Raman studies (Fig. 4b). The Raman bands found at 1354 and 1582 cm^{-1} pertained to D and G bands, respectively. The 1354 cm^{-1} band corresponded to sp^3 hybridized carbon atoms with A_{1g} symmetry of structure distortion whereas the graphitic band at 1582 cm^{-1} represented the sp^2 hybridization of the carbon atoms owing to the first order scattering of the E_{2g} mode[16,47]. The intensity ratio (I_D/I_G) for the RGO was found to be about 0.97 and the crystallite size was calculated to be about 19.8 nm using Eq. 9.

$$La(nm) = (2.4 \times 10^{-10})\lambda_1^4 (I_D/I_G)^{-1} \quad (9)$$

where λ_1 is the wavelength of laser (nm), I_D and I_G represent the band intensities[21]. In the spectrum of Cys-RGO, the additional bands seen at 498, 670 and 827 cm^{-1} were assigned to S–S stretching, C–S stretching and S–H bending, respectively, whereas bands found at 2440, 2918 and 2970 cm^{-1} were due to S–H stretching, C–H stretching and CH_2 asymmetric stretching, respectively[48]. Besides this, the decline in the intensity of D and G bands in Cys-RGO spectrum indicated functionalization of RGO via Cys.

The BET studies on the Cys-RGO were conducted to determine the surface area and porous structure. The pore size distribution and adsorption-desorption (N_2) isotherm graph of Cys-RGO is shown Fig. S1. We obtained good surface area of 31.53 $m^2\ g^{-1}$ with mesoporous structure of Cys-RGO. The volume of pores and average pore size of Cys-RGO were calculated to be as 0.119 cc g^{-1} and 8.87 nm, respectively. The mesoporous structure of Cys-RGO was confirmed by pore size distribution spectra (inset of Fig. S1b). The observed mesoporous structure and high surface area enabled improved immobilization of the desired biomolecules on the transducer surface resulting in enhanced stability and output signal of a biosensor.

3.3 Surface functionalization studies

Fourier transform infrared studies were carried out to investigate the surface modification of graphene-hydrogel (Fig. 4c). In the spectrum of RGO, peaks found at 1577 and 1730 cm^{-1} were due to conjugated C=C stretching and C=O stretching vibrations of carboxylic group, respectively. The peaks seen at 1226-1401, and 1068 cm^{-1} were assigned to C–H bending and C–O stretching, respectively, while peaks found at 2998 and 3458 cm^{-1} pertained to C–H stretching and O–H stretching vibrations, respectively[49]. For Cys-RGO, the peaks found at 850-961, 1198 and 1340 cm^{-1} corresponded to C–S

View Article Online
DOI: 10.1039/C9LC00751B

stretching, N–CS stretching and C=N stretching vibration, respectively, whereas peak seen at 2584 cm^{-1} was related to terminated thiol (S–H) group of Cys present in Cys-RGO. Further, peaks at 1585 and 1626 cm^{-1} were due to N– H (amide II) and C=O (amide I). In this case, NH_2 group of L-cysteine reacted with –COCl groups onto the surface of thionyl chloride modified RGO–COCl and were converted to NHCO graft[50,51]. In the spectrum of Cys-RGO/Au, the S–H peak at 2584 cm^{-1} perhaps disappeared due to the formation of S–H bond that was directed to the formation of S–Au bond. This indicated that thiol-terminated Cys-RGO molecules were perhaps bound onto the Au electrode surface. After the antibodies immobilization on the surface of Cys-RGO/Au electrode, the peaks were shifted slightly and the additional peaks found at 1530 and 1688 cm^{-1} were perhaps owing to the formation of amide I and amide II bonds between the antibodies and Cys-RGO indicating immobilization of the antibodies on Cys-RGO/Au electrode.

The X-ray photoelectron spectroscopy (XPS) studies were conducted to confirm the surface functionalization of cMAb and Cys-RGO. A wide-scan XPS survey of Cys-RGO film showed the occurrence of carbon (C), nitrogen (N), oxygen (O) and sulphur (S) peaks at the binding energies of 284.1, 398, 531.08 and 162.32 eV, respectively (Fig. 5a). The C1s spectra of Cys-RGO revealed the binding energies at 283.43, 284.35, 285.31, 286.66 and 287.94 eV due to C=C, C–C (graphite), C–S and C–N, –C–O and HO–C=O (carboxylic) functional groups, respectively (Fig. 5b)[52,53]. In the N1s spectrum of Cys-RGO (Fig. 5c), the 397.41 eV peak was observed due to the presence of N–O group, while the peaks at 398.40 and 399.32 eV were attributed to the NH_3^+ species. The peak found at 400.23 eV indicated the binding energy of N in the formation of (NC=O) bond in between the Cys and RGO. The O1s spectra (Fig. 5d) revealed peaks at 530.11, 531.77 and 533.3 eV that were assigned to C=O, C–O and O–H groups, respectively. The peaks observed at 161.78 and 163.02 eV pertained to the $S2p_{3/2}$ (S–H) and $S2p_{1/2}$ (S–H) groups, respectively, a validation that the RGO surface was functionalized with Cys (Fig. 5e)[54–56]. These results are consistent with the Raman results (Fig. 4b).

After deposition of Cys-RGO hydrogel on Au, a wide scan XPS survey exhibited the presence of elements, Au, S, O, N and C (Fig. 5f). The peak at 84.12 eV was assigned to gold. The high-resolution spectrum of S2p (Fig. 5g) contained a pair of peaks at 161.21 and 162.33 eV that arose due to S–Au bonding at the Au surface whereas the 166.11 eV peak was attributed to S–H and S–O–C bonding. The deconvoluted Au4f spectrum (Fig. 5h) revealed two pair of peaks in the $Au4f_{7/2}$ and $Au4f_{5/2}$ doublet. The 83.93 and 87.68 eV peaks were due to Au^0. And the peaks found at 85.71 and 89.63 eV were due to Au–S coupling[56,57].

A wide-scan XPS survey for cMAb/Cys-RGO/Au film revealed the presence of elements, C, N, O, S and Au (Fig. 5i). The C1s spectra for cMAb immobilized Cys-RGO shown in Fig. 5j revealed an additional

peak at 286.95 eV indicating the formation of amide (O=C–NH–) bonds between the $–NH_2$ groups of the cMAb and –COOH groups of Cys-RGO[53]. In addition, the peak for carboxylic groups at ~287.94 eV (Fig. 5b) was found to be absent in Fig. 5j confirming the conversion of –COOH groups to amide groups ($CONH_2$). The peak arising due to amide bond (O=C–NH–, 286.95 eV) was shifted to lower binding energy position (~1 eV) than the peak due to carboxylic group (O=C–OH, 287.94 eV) after covalent immobilization of cMAb on the Cys-RGO surface. The small shift in the lower binding energy was perhaps due to the electron donation from the adjacent nitrogen atom of amide groups. It appeared that the p orbitals of nitrogen atom donate an electron in the conjugation, resulting in the shift of the binding energy position [4]. Also, the peaks related to graphitic (C=C, C–C) and NC=O were slightly shifted to lower binding energies due to the immobilization of cMAb on the Cys-RGO surface. The N1s spectra of antibody immobilized Cys-RGO is shown in Fig. 5k. The peaks at 398.28, 399.89 and 400.82 pertained to –N= and the amide bond (–HN–C=O), respectively. Fig. 5l shows the O1s spectra for antibody immobilized Cys-RGO. The binding energy position of O1s was slightly shifted to lower binding energy indicating the formation of amide –CONH groups from the conversion of the COOH groups. These results are consistent with the FTIR results (Fig. 4c).

3.4 Microscopic studies

FESEM was used to determine the structural morphology of the porous Cys-RGO hydrogel. Fig. 6 (a and b) show the FESEM images of RGO sheets. The RGO sheets were obtained as multilayers, folded and agglomerated. The multi-layered thicker sheets of RGO were perhaps formed by stacking of layers of π–π interaction among the separate sheets. Fig. 6(c, d and e) revealed the growth of porous Cys-RGO hydrogel microstructure that was assigned to the self-assembly of RGO nanosheets and L-cysteine in aqueous colloidal solution. The porous microstructures of Cys-RGO hydrogel was inter-connected to each other due to the covalent interface among the –COOH groups of RGO and $–NH_2$ group of Cys resulting in formation of a porous dense network. This is consistent with the results of FTIR, Raman and XPS studies. Fig. 6f exhibits the image of cMAb/Cys-RGO arising due to a morphological change at the Cys-RGO surface occurring due to the formation of amide bonding between cMAb and Cys-RGO hydrogel.

The energy-dispersive X-ray (EDX) analysis was carried out to investigate the elemental composition of C, N, O and S in Cys-RGO hydrogel (Fig. S2). The atomic and weight percentage of C, N, O and S in Cys-RGO were found to be 50.2%, 11.1%, 15.2% and 23.5% and 41.3%, 10.2%, 17.5% and 31.0%, respectively (Fig. S2, inset).

Transmission electron microscopy (TEM) was used to investigate the surface structure and crystalline nature of RGO sheets and Cys-RGO hydrogel (Fig. S3). The folding, thin layers, and wrinkles

View Article Online
DOI: 10.1039/C9LC00751B

of the RGO nanosheets could be seen in Fig. S3a and b, respectively. The presence of basal planes and edges in RGO structure were owing to the interface of oxygen (O−) having bonds in the adjoining layers. Fig. S3c shows the high-resolution transmission image with lattice fringes and (002) reflection planes of RGO (inset of Fig. S3c) that occurred in the selected area electron diffraction (SAED) pattern owing to the crystalline structure of RGO that was in agreement with the results of XRD studies. The RGO was functionalized by L-cysteine as shown in Fig. S3d-f. It appeared that the amine groups of L-cysteine reacted with the carboxyl groups of RGO resulting in the formation of covalent bonds[42]. The hierarchical cross-linked structure of Cys-RGO hydrogel can be clearly seen in Fig. S3e and f.

4. Electrochemical characterization

Cyclic voltammetry (CV) measurements were performed to investigate the redox and electrolytic interfacing activity of RGO, Cys, Cys-RGO and cMAb/Cys-RGO electrode in 50 (mM) PBS (pH 7.4) having 5 mM ferro-ferricynide redox mediator at 20 mV/s scan rate (Fig. 7a). The electrochemical parameters such as heterogeneous electron transfer rate (K_s), anodic peak current (I_{pa}), surface diffusion coefficient (D) and surface concentration (I^*) were determined by equations S1–S3 (Supporting information) and are summarized in Table S1. The RGO showed higher electrochemical current of 669 µA due to larger surface area and superficial heterogeneous electron transfer properties of the RGO[49]. The Cys electrode showed an anodic peak current of 299.3 µA, while with the Cys modification with RGO, the current value was found to increase to 438.2 µA. This is owing to the porous structure and higher surface area of Cys-RGO hydrogel, improved electron conductivity of RGO, resulting in enhanced rate of diffusion of electrolytic ions compared to the Cys electrode. At the Cys-RGO electrode, a maximum heterogeneous electron transfer rate (K_s) was found as compared to the Cys and cMAb/Cys-RGO electrodes (Table S1). After immobilization of cMAb with BSA on Cys-RGO, the redox current decreased to 228.4 µA and a higher peak-to-peak separation potential was found due to the non-conducting layer of cMAb and BSA molecules on the bioelectrode. The transportation of generated electrons in the electrolytic medium was hindered due to the bulky biomolecular structure of BSA-cMAb on Cys-RGO surface.

The CV response of the cMAb/Cys-RGO immunoelectrode was measured as a function of scan rate (10-100 mV/s) (Fig. 7b) in the presence of a redox mediator. With increasing scan rates, the redox peak current increased linearly along with a linear shift in the peak potential. However, the peak current is inversely proportional to the square root of scan rate implying a diffusion-controlled process. A higher surface concentration of redox species was found for the RGO (5.97×10^{-6} mole cm^{-2}). The high aspect ratio of the RGO electrode delivered maximum surface diffusion coefficient (34.37×10^{-2} cm^2 s^{-1}), owing to delocalized π-electrons in six carbon member rings of RGO and greater

electron transportation. For the Cys electrode, the values of surface concentration and diffusion coefficient decreased to 2.66×10^{-6} mole cm^{-2} and 6.87×10^{-2} cm^2 s^{-1}, respectively, due to insulating layer of Cys at the Au surface. However, the Cys-RGO electrode showed higher surface concentration and surface diffusion coefficient 3.91×10^{-6} mole cm^{-2} and 14.73×10^{-2} cm^2 s^{-1}, respectively compared to that of the Cys electrode. It could be due to the mesoporous structure of Cys-RGO hydrogel and covalent interaction between Cys and RGO resulting in improved transfer of electrons during electrolytic reactions. In addition, surface concentration and diffusion coefficient were found to decrease to 2.03×10^{-6} mole cm^{-2} and 4.1×10^{-2} cm2 s^{-1}, respectively, for cMAb/Cys-RGO bioelectrode. This was perhaps due to the extremely anisotropic tunnelling of electrons arising due to cross linking of the Cys between the Au electrode and the RGO structure. The choice of Cys-RGO hydrogel facilitated a larger surface with porous structure and a greater K_s compared to the use of Cys only, resulting in enhanced biosensor efficiency.

Electrochemical impedance spectroscopy (EIS) technique was used to determine the interfacial activity of the fabricated sensor material-electrolyte interface in the presence of a sinusoidal AC signal. Fig. S4a shows the Nyquist plot for the Cys-RGO by the EIS method to determine R_{ct} values. Fig. S4b reveals the EIS spectra obtained for the fabricated biosensor. We found the low R_{ct} value of 40.5 Ω at the RGO electrode. The formation of self-assemble monolayer of Cys on Au electrode (Cys/Au) led to increased value of R_{ct} to 140.43 Ω. Due to functionalization of RGO with Cys, the R_{ct} value decreased to 98.21 Ω at the Cys-RGO electrode. After immobilization of the antibodies, the Cys-RGO/Au electrode showed an increased value of R_{ct} owing to the formation of insulating layer of antibodies at its surface. The cMAb/Cys-RGO electrode revealed the maximum R_{ct} value of 352.3 Ω among all the fabricated sensor electrodes.

4.1 Dual-modality detection of cMb

In the electrochemical mode of detection, the DPV technique was employed to detect cMb using fabricated microfluidic sensor (Fig. 3**).** First, we used a microfluidic chip without RGO hydrogel (cMAb/Cys/Au) wherein various concentration of standard cMb (0.004–1000 ng mL^{-1}) introduced sequentially (Fig. 7c). The response peak current was found to decrease with increasing cMb concentration. The specific cMAb on the sensor surface captured cMb via site-specific paratopes and epitope interactions while cMb molecules exposed to the sensor surface, led to the formation of antigen-antibody immunocomplex insulating layer that hindered the transport of electrons through redox conversion of ferro/ferricynide in PBS electrolyte solution resulting in decreased current (I). Fig. 7d shows the calibration plot obtained for the microfluidic bioelectrode (cMAb/Cys/Au) wherein the cMb concentrations were plotted against current and the calibration equation as given by Eq. 10.

View Article Online
DOI: 10.1039/C9LC00751B

$$I\ (\mu A) = 1.637\ \mu A - 0.805\ \mu A \times (cMb, ng\ mL^{-1}),\ r^2 = 0.981 \quad (10)$$

It was found that with increased cMb concentration from 0.004 to 0.04 ng mL^{-1}, the sensor response current did not decrease significantly. However, in the higher concentration range of cMb, the sensor showed significant reduction of current. The sensitivity of the cMAb/Cys/Au-based microfluidic bioelectrode was determined to be 134.16 µA/(ng mL^{-1})/cm^2 with a low LOD of 40 pg mL^{-1}.

For Fig. 8a and c, we carried out DPV measurements using another microfluidic device with RGO hydrogel (cMAb/Cys-RGO/Au) where the various concentrations of cMb were sequentially introduced in the same microfluidic channel (Fig. 3). The microfluidic bioelectrode (cMAb/Cys-RGO/Au) shows the overlay of DPV spectra (Fig. 8a) with different cMb concentration of the standard sample ranging from 0.004 to 1000 ng mL^{-1}. An important observation about the cMAb/Cys-RGO/Au sensor was that the response current decreased significantly in the range of (101.6–22.2 µA) with increasing cMb concentration (0–1000 ng/mL). However, the cMAb/Cys/Au sensor showed decreased response current values (59–18.7 µA) compared to that of the cMAb/Cys-RGO/Au sensor resulting in a higher sensitive cMAb/Cys-RGO/Au sensor. The calibration equation (11) with regression coefficient of $r^2 = 0.988$ was obtained by the plot of cMb concentration verses peak current, (Fig. 8b).

$$I\ (\mu A) = 1.838\ \mu A - 1.175\ \mu A \times cMb\ (ng\ mL^{-1}),\ r^2 = 0.988 \quad (11)$$

With the incorporation of RGO hydrogel in this sensor, the sensitivity increased to about double (196.66 µA/(ng mL^{-1})/cm^2) and a low LOD of 4 pg mL^{-1} was obtained compared to that obtained for sensor without RGO hydrogel (134.16 µA/(ng mL^{-1})/cm^2 and 40 pg mL^{-1}, respectively). The high sensitivity was due to the interconnected porous microstructure of Cys-RGO hydrogel allowing the electrolyte to diffuse freely in the porous network, resulting in high electron transportation from the surface of porous Cys-RGO hydrogel electrode in the electrolyte solution. In addition, porous network, lager surface area and abundant groups such as –COOH, –OH at RGO hydrogel surface led to enhanced binding of cMAb on the electrode surface resulting in high surface reactivity with cMb, thus, this sensor showed a higher sensitivity and a low LOD.

4.2 Monitoring real serum samples

Serum samples of cardiac patients were collected from a local hospital (Kamineni Hospital, LB Nagar, Hyderabad, Telangana) as per pre-approved clinical protocols. The cMb concentration in serum of a cardiac patient was determined against the standard enzyme linked immunosorbent assay (ELISA) detection technique. We made numerous concentrations of cMb with the known concentrations of cMb in the serum by diluting in 5 mM PBS (pH 7.4) solution and then, these serums were used for cMb sensing using the fabricated dual-modality microfluidic device. The microfluidic chip with RGO

View Article Online
DOI: 10.1039/C9LC00751B

hydrogel (cMAb/Cys-RGO/Au) was used to detect the cMb concentrations in serum sample (0.04–500 ng mL^{-1}) (Fig. 8c). As the cMb concentration increased, the peak current was decreased. Fig. 8d shows the calibration response plot for cMAb/Cys-RGO/Au microfluidic bioelectrode between the serum cMb concentration and peak current with regression coefficient of $r^2 = 0.985$, Eq. 12.

$$I\ (\mu A) = 1.85\ \mu A - 1.22\ \mu A \times \text{serum cMb (ng mL}^{-1}\text{)},\ r^2 = 0.985 \quad (12)$$

The sensitivity of the cMAb/Cys-RGO/Au microfluidic device for serum cMb was obtained as 203.66 $\mu A/(ng\ mL^{-1})/cm^2$ which was slightly higher than the sensitivity of standard cMb sample (196.66 $\mu A/(ng\ mL^{-1})/cm^2$) with a low LDO of 0.04 ng mL^{-1}. Table 1 compares the performance of these sensors alongwith those reported in literature.

Fig. 8e shows the sensing plot obtained between standard cMb and real serum cMb (0.04–500 ng mL^{-1}). We found that the relative standard deviation (RSD) for three repeated DPV measurements was as low as 4.48% and 5.89% for standard and serum samples, respectively (Fig. 8e). We determined the sensor recovery of serum cMb samples with the lab-prepared standard samples. The recovery values of human serums were found to be between 90.46–104.25% indicating good performance of the fabricated microfluidic device. Further, intra-replicate variabilities of this sensor were calculated for standard and serum samples. It was observed that the intra-assay coefficient of variation was between 4.72–7.29% for standard samples and 3.8–8.79% for real serum samples, respectively. The recovery and intra-assay coefficient of variation (CV) details of the sensor was included in the Table 2.

Further, we determined the sensor performance using 100% serum spiked with known concentration of cMb and compared with standard cMb samples. The serum samples (100%) of five cardiac patients were collected from local hospital (Kamineni Hospital, LB Nagar, Hyderabad, Telangana) as per pre-approved clinical protocols. First, the cMb concentration in 100% serum of five cardiac patients was determined by the standard enzyme linked immunosorbent assay (ELISA) detection technique. Then, these five serums samples obtained from cardiac patients (115, 196, 348, 415 and 530 ng mL^{-1}) were used for cMb sensing using the fabricated microfluidic device (Fig. S5a). The peak current decreased as the cMb concentration increased in serum. Fig. S5 b shows the overlay of DPV spectra with different cMb concentration of the standard samples (115, 196, 348, 415 and 530 ng mL^{-1}). In case of 100% serum samples, the response current decreased significantly in the range of (35.8–20.1 µA) as the cMb concentration increased in serum (115–530 ng mL^{-1}). However, in case of standard cMb (115–530 ng mL^{-1}), the sensor showed decreased response current values (37.13–22.52 µA). As a result, the device detecting performance for the 100% serum spiked (response current range, 35.8–20.1 µA) and standard cMb (response current range, 37.1–22.52 µA) remained the almost same.

View Article Online
DOI: 10.1039/C9LC00751B

Fig. S5c. shows the sensing plot obtained between standard and 100% serum cMb samples of five cardiac patients (115, 196, 348, 415 and 530 ng mL^{-1}). We found that the relative standard deviation (RSD) for three repeated DPV measurements was as low as ±2.23% and ±2.97% for standard and serum samples, respectively (Fig. S5 c). We evaluated the sensor recovery performance using both serum cMb and standard cMb samples. The recovery values of human serums were found to lie in the range, 89.96–96.42% indicating good sensing ability of the fabricated microfluidic device. Further, intra-replicate variabilities of this sensor were calculated for both standard and serum samples. It was observed that the intra-assay coefficient of variation varied from 2.52 to 8.1% and from 3.98 to 8.92% for standard and real serum samples, respectively. The results of sensing performance with 100% serum samples and the recovery studies of the sensor are included in the Table S2.

We conducted a control study using the microfluidic sensor having Cys-RGO/Au electrode (Fig. 8f) without immobilization of cMAb. When different concentrations of standard cMb samples were introduced in the chip, we did not observe any notable change in the output signals of current. Without immobilization of cMAb in the sensor surface underwent non-specific interactions of cMb at the Cys-RGO/Au surface resulting in unchanged output signal. However, a slight variability in the output signal using Cys-RGO/Au sensor was due to the non-specific assignation of cMb (0.2 to 500 ng mL^{-1}). Further, we conducted a control experiment using Cys-RGO/Au electrode without incorporating antibodies in presence of 100% serum samples of five cardiac patients (115, 196, 348, 415 and 530 ng mL^{-1}). When cMb serum concentrations of five cardiac patients (115, 196, 348, 415 and 530 ng mL^{-1}) were introduced in the device, we did not observe any significant change in the sensor output currents (Fig. S6). Without cMAb, Cys-RGO/Au sensor was not able to capture the cMb molecules in the serum, thus, output currents remain unchanged. However, a slight variability (%RSD, 4.29) in the output signal with respect to baseline may be due to the non-specific assignation of cMb. During this measurement, no redox peak in the potential range of -0.2 to 0.8 V vs Ag/AgCl was observed. It appeared that the serum components did not significantly react on the sensor surface.

In the plasmonic mode of detection, the SPR technique was employed to detect cMb concentration via antigen-antibodies interaction on microfluidic sensor surface (Fig. 3). An SPR sensorgram plot showed the *in-situ* immobilization of cMAb immobilization on Cys-RGO/Au surface via EDC-NHS chemistry (Fig. 9a). A thin layer of Cys-RGO hydrogel on Au surface was used as a baseline and stabilized by introducing PBS solution (Step 1). Then, 50 µL of EDC-NHS solution was injected into the microchannel via automatic sequence on the surface of Cys-RGO/Au for 360 s to activate –COOH groups on Cys-RGO. In this step, the SPR angle was found to be changed due to the EDC-NHS coupling on the surface of Cys-RGO/Au (Step 2) and the surface was washed with PBS (Step 3). To *in-situ* immobilize the cMAb, 30 µL of cMAb was injected onto the EDC-NHS modified Cys-RGO/Au surface

View Article Online
DOI: 10.1039/C9LC00751B

for 30 min resulting in the change of SPR angle (Step 4). The change in the SPR angle after cMAb immobilization (Fig. 9b) confirmed the attachment of cMAb on the Cys-RGO/Au surface. The surface was regenerated by introducing PBS for 120 s (Step 5) and then, the cMAb/Cys-RGO/Au surface was treated with BSA for 300 s to block non-specific binding (Step 6). Finally, the BSA-cMAb/Cys-RGO/Au biosensor surface was washed with PBS (Fig. 9a, Step 7).

The density (surface) of the immobilized cMAb molecules on Cys-RGO/Au was determined using Eq. 13

$$A = \frac{\Delta \text{ Response } [\text{m}^{\text{o}}]}{\text{Conversion factor}[\text{m}^{\text{o}}.(\text{mm}^2/\text{ng})]} \qquad (13)$$

where A is the surface density of the immobilized cMAb. The surface density of cMAb on the cMAb/Cys-RGO/Au sensor was obtained as 4.93 ng mm^{-2}. The quantity of cMAb immobilized onto the cMAb/Cys-RGO/Au surface was obtained as 38.91 ng via Eq. 14.

$$A\text{mount} = \text{Surface density } (\text{ng}/\text{mm}^2) \times \text{Surface area } (\text{mm}^2) \qquad (14)$$

The number of cMAb bound on the cMAb/Cys-RGO/Au surface was calculated using Eq. 15.

$$N = \frac{\text{Amont(ng)}}{\text{Molar mass(g/mol)}} \times \frac{10^{-9}(\text{g})}{(\text{ng})} \times 6.022 \times 10^{23}(\text{mol}^{-1}) \qquad (15)$$

where N represents the number of cMAb molecules on the Cys-RGO/Au, was obtained to be 1.38×10^{15}.

Further, we measured the SPR response of the microfluidic chip using 5 mM PBS (PH 7.4) as function of cMb concentrations (0.01–1000 ng mL^{-1}). After completion of the cMb binding time (360 s) then the PBS was injected into the microchannel to obtain same environments before the binding phase. The change in the value of SPR angle before and after the interaction phase was used to determine the binding of cMb on the sensor surface. Fig. 9c shows the SPR sensogram obtained for the detection of various concentration of cMb. The SPR angle increased during association with respect to time due to site-specific binding of cMb with cMAb on Cys-RGO/Au surface. The change in the SPR angle was found at the cMAb/Cys-RGO/Au microfluidic surface with cMb when the cMAb/Cys-RGO/Au was excited by the normal incident light. As the cMb concentration increased, the response of the SPR angle was increased due to the enhancement of kinetic binding between cMb and cMAb conjugated Cys-RGO hydrogel. Fig. 9d shows calibration plot obtained between the SPR angle and cMb concentration. In the SPR modality of cMb sensing showed a dynamic range of 0.01–1000 ng mL^{-1} with regression coefficient of 0.983. The SPR sensing revealed LOD of 10 pg mL^{-1} with a sensitivity of 42.86

View Article Online
DOI: 10.1039/C9LC00751B

m^o/(ng mL^{-1}) while DPV sensing showed a sensitivity of 196.66 µA ng mL^{-1} cm^{-2} for a dynamic concentration of (0.004−1000 ng mL^{-1}) with a LOD of 4 pg mL^{-1}.

The rate constants K_a and K_d for the binding of cMb–cMAb using this sensor were calculated to be as 4.93 ± 0.2 × 10^5 M^{-1} s^{-1} and 1.37 ± 0.08 × 10^{-4} s^{-1}, respectively. The equilibrium constant (K_A=K_a/K_d) was determined as 3.59 × 10^9 M^{-1}. The microfluidic chip provides higher k_a and lower k_d values with a LOD of 0.01 ng mL^{-1} (10 pg mL^{-1}) compared to those obtained using other nanomaterial such as gold nanoparticle (K_a=1.20 ± 0.01 × 10^5 M^{-1} s^{-1} and K_d=5.7 ± 0.5 × 10^{-4} s^{-1}) with a LOD of 0.18 ng mL^{-1} [58].

4.3 Selectivity studies

The selectivity test of the sensor was conducted using cMb (100 ng mL^{-1}) in the presence of similar biomolecules such as creatine kinase-MB (100 ng mL^{-1}), C-reactive protein (CRP) (100 ng mL^{-1}), cardiac troponin I (cTnI) (100 ng mL^{-1}), cardiac troponin T (cTnT) (100 ng mL^{-1}), troponin C (TnC) (100 ng mL^{-1}) and with haemoglobin (Hb) (100 ng mL^{-1}) which has similar configuration with cMb. Both the cMb and Hb have oxygen (O_2) ligands and are iron containing proteins and globular proteins. (Fig. 10a). The sensor baseline was set to 39 µA when the sensor was exposed to 100 ng mL^{-1} of cMb without any interfering biomolecules. By adding different interfering molecules into cMb (100 ng mL^{-1}), the sensor did not show any significant change in the output signal as compared to baseline (Fig. 10b). The obtained low RSD (4.38%) indicated that this sensor is highly specific in presence those interfering biomolecules.

4.4 Reproducibility and stability studies

For the reproducibility test, we fabricated four identical sensors using cMAb/Cys-RGO/Au. These biosensors were employed to quantify 100 ng mL^{-1} concentration of cMb using DPV technique. Fig. 10c reveals the DPV spectra of four identical sensors for quantify 100 ng mL^{-1} concentration of cMb. Inset of Fig. 10c, histogram plot for peak currents with respect to four identical biosensors tested. Output signals of these four sensors provide a low relative standard deviation (RSD = 5.14%). The results indicate good reproducibility due to the lithographic fabrication of sensor. In addition, we determined the inter-assay CV of four identical sensors at a function of 100 ng mL^{-1} concentration of cMb. The inter-assay CV was found to lie in the range, 3.56–6.32% for four identical sensors indicating good reproducibility of the sensor. The details of inter-assay CV of the four identical sensors were comprised in the Table 3.

The stability of the biosensor was evaluated by measuring DPV response at a regular interval over six weeks. Fig.10d reveals the DPV responses of the biosensor for cMb (5 ng mL^{-1}) recorded once

View Article Online
DOI: 10.1039/C9LC00751B

a week over a six-week period. After each DPV measurement, the sensor was washed with PBS solution and was put in storage at 4 °C to maintain the activity of sensor surface. This sensor showed a stable DPV current response (Fig. 12d), inset of Fig. 10d shows the DPV spectra in the presence of 5 ng mL^{-1} cMb. After four weeks, a small reduction in output current was observed with the RSD (N=3) of 3.37%.

The developed dual-modality microfluidic biosensor integrates both electrochemical and SPR detection techniques on a same substrate by incorporating mesoporous Cys-RGO hydrogel for biomonitoring of cMb biomarker and has following novelties:

- The incorporated dual-modality Cys-RGO hydrogel microfluidic structure potentially will provide improved sensing reliability, owing to the capability of the sensor to create two readouts for a specific interaction of antigens with antibodies at the transducer surface.
- The detection via electrochemical method is beneficial due to the presence of Cys-RGO hydrogel on the working electrode surface, allowing effective radial diffusion of redox species. This sensor has a low limit of detection (LOD) of a pg mL^{-1} for biomonitoring of cMb biomarker using the DPV mode with a recovery values of serums cMb were between 90.46–104.25% and provides an inter-assay and intra-assay accuracy of less than 9%, which will be clinically helpful to the diagnosis of early-stage heart stroke.
- The plasmonic mode of detection exhibits a higher LOD of 10 pg mL^{-1} for cMb and allows kinetic binding of antigens-antibodies interactions at the same electrode surface material (Cys-RGO). To track the capability of biomolecular interaction via association and dissociation process will significantly assist the researcher to improve recognition of molecular behaviors for enhanced interaction of target analyte for a specific antibody.

5. Conclusions

We have fabricated a highly sensitive amperometric and SPR microfluidic biosensor for the detection of serum cMb concentrations and antigen–antibodies binding kinetics for cMb. The biosensor has been fabricated by integrating the mesoporous Cys-RGO hydrogel at microfluidic WE and has been used to quantify cMb concentration via DPV technique. The SPR method has been used to calculate the antigen-antibodies binding kinetics at the cMAb/Cys-RGO/Au bioelectrode. The covalent attachment among the Cys-RGO hydrogel and Au coated glass substrate via S–Au bonding provided facile modification of the WE surface. The cMAb molecules immobilized on the Cys-RGO/Au surface allowed precise detection of cMb even in the presence of other interfering biomolecules. The high surface, mesoporous structure of Cys-RGO hydrogel and abundant of functional groups at Cys-RGO contributed to the loading of higher number of antibodies resulting in enhanced sensitivity, high

View Article Online
DOI: 10.1039/C9LC00751B

selectivity and more kinetic binding. The Cys-RGO functionalized cMAb has shown greater value of K_a and K_d rate constant ($4.93 \pm 0.2 \times 10^5$ M^{-1} s^{-1} and $1.37 \pm 0.08 \times 10^{-4}$ s^{-1}, respectively) of cMb–cMAb indicating strong affinity between cMAb/Cys-RGO and cMb molecules. Thus cMAb/Cys-RGO/Au microfluidic biosensor showed dynamic detection concentration range (0.004−1000 ng mL^{-1}) of cMb with high sensitivity of 196.66 µA ng mL^{-1} cm^{-2} (amperometric) or 42.86 m^o/(ng mL^{-1}) (SPR) and good specificity. This biosensor exhibited the LOD of 4 pg mL^{-1} of cMb via DPV mode and SPR sensor revealed an LOD of 10 pg mL^{-1}. Efforts should be made to explore the application of this microfluidic chip for monitoring of other clinically important biomolecules and other physiological parameters including low density lipoprotein, triglycerides, creatine kinase-MB and troponin I etc.

Working electrodes	Detection techniques	Detection range (ng/mL)	LOD (ng/mL)	Reference
GO/CNT	CV	1–4000	0.34	[59]
SAM/Au	EIS	10–650	5.2	[60]
AuNPs@rGO/SPE	DPV	1–1400	0.67	[61]
Anti-MYO/GQDs	EIS & DPV	0.01–100	0.01	[62]
EXO I/aptamer-Au	DPV	1.75–700	0.45	[63]
Ab-Mb/AuNPs/APTES/ITO	EIS	10 –1000	2.7	[64]
AuNPs/BNNSs/FTO	DPV	10^2–10^5	34.6	[65]
MWCNTs/SPEs	EIS	0.1–90	0.08	[66]
cMAb/Cys-RGO/Au microfluidic chip	SPR	0.01–1000	0.01	Present work
cMAb/Cys-RGO/Au microfluidic chip	DPV	0.004−1000	0.004	Present work

Table 1. The characteristics of the cMAb/Cys-RGO/Au biosensors alongwith those stated in literature for cMb quantification.

View Article Online
DOI: 10.1039/C9LC00751B

S.No	cMb Conc. (ng mL^{-1})	Peak current (µA) obtained for standard cMb sample	Peak current (µA) obtained for serum cMb sample	% CV for standard sample (N=3)	% CV for serum sample (N=3)	Recovery (%)
1	0.04	90.0	91.5	4.72	3.80	101.66
2	0.2	82.3	85.8	5.13	4.48	104.25
3	5	62.4	63.9	6.93	6.16	102.41
4	25	52.0	49.0	6.14	8.06	94.24
5	100	40.1	37.0	7.76	7.13	92.27
6	500	26.2	23.7	7.29	8.79	90.46

Table 2. Determination of recovery and intra-assay coefficient of variation (CV) between peak current (µA) obtained for synthetic (standard) and real serum sample of cMb for different concentration using cMAb/Cys-RGO/Au sensor.

Sensors	cMb Conc. (ng mL^{-1})	Peak current (µA) obtained for cMb sample	% CV (N=3)
1	100	44.6	5.19
2	100	39.9	4.11
3	100	45.8	3.56
4	100	41.8	6.32

Table 3. Determination of inter-assay coefficient of variation (CV) of four identical sensors, using the peak current (µA) obtained at 100 ng mL^{-1} cMb concentration.

Acknowledgements

The authors are thankful to Dr. Inayatullah Ghori, Kamineni Hospital, LB Nagar, Hyderabad, India for providing the clinical sample. BDM thanks the Science & Engineering Research Board (Govt. of India) for the award of a Distinguished Fellowship (SB/BF-011/2019).

Associated content

Supplementary information

Chemicals and reagents, Instrumentation, Device fabrication, UV-visible studies, BET, EDX of Cys-RGO hydrogel, TEM, Electrochemical Characterization, SPR Measurements, table for electrochemical

View Article Online
DOI: 10.1039/C9LC00751B

parameters of various fabricated electrodes, DPV response of the microfluidic device in presence of 100 % serum cMb, Table for recovery and intra-assay coefficient of variation (CV) between peak current (μA) obtained for synthetic (standard) and 100% serum sample of cMb, Control experiment using Cys-RGO/Au electrode without incorporating antibody in presence of 100% serum spiked.

Figure captions

Schematic: Graphical abstract.

Fig. 1. Proposed mechanism for the synthesis of Cys-RGO hydrogel: (a) Structure of RGO Sheet. (b) RGO modified via thionyl chloride ($SOCl_2$). (c) Structure of porous Cys-RGO hydrogel.

Fig. 2. (a-b) Step-wise illustration for the fabrication of dual-modality Cys-RGO microfluidic biosensor. (c) Fabricated three electrode patterns wherein Cys-RGO hydrogel is deposited on the WE (Au).

Fig. 3. (a) Schematic demonstration of an incorporated dual-modality Cys-RGO hydrogel microfluidic biosensor chip for the detection of cMb. (b) A photograph of the nanoengineered integrated dual-modality mesoporous Cys-RGO hydrogel microfluidic biosensor chip. (c) SEM image of the integrated Cys-RGO hydrogel. (d) Incorporated dual-modality Cys-RGO hydrogel sensor action revealing coupling of light and voltage source to measure electrochemical and SPR signals.

Fig. 4. Characterization of ROG, Cys-RGO hydrogel and cMAb/Cys-RGO: (a) XRD spectra of RGO. (b) Raman spectra of RGO and Cys-RGO hydrogel. (c) FTIR spectra of RGO, Cys-RGO, Cys-RGO/Au and cMAb/Cys-RGO/Au.

Fig. 5. XPS studies for Cys-RGO hydrogel and Cys-RGO/Au electrode. (a) Wide-scan spectra for Cys-RGO, shows the presence of C, N, O and S elements, (b) C1s spectra, (c) N1s spectra, (d) O 1s spectra and (e) S2p spectra. (f) Wide-scan spectra for Cys-RGO/Au electrode shows the presence of additional Au element and thiol-gold (S-Au) bonding, (g) S2p spectra and (h) Au4f spectra.

Fig. 6. FESEM characterization of the RGO, Cys-RGO hydrogel and cMAb/Cys-RGO hydrogel. (a and b) FESEM images of RGO sheets. (c, d and e) FESEM images of Cys-RGO hydrogel. (f) cMAb immobilized Cys-RGO hydrogel.

Fig. 7. (a) CV responses for the RGO, Cys, Cys-RGO hydrogel electrode and cMAb/Cys-RGO bioelectrode in PBS containing 5 mM $[Fe(CN)_6]^{3-/4-}$ as redox mediator. (b) CV responses of the cMAb/Cys-RGO/Au sensor by varying scan rate. (c) Differential pulse voltammetry (DPV) response of the microfluidic chip without RGO hydrogel (cMAb/Cys/Au) by varying cMb concentration from 0.004 to 1000 ng/mL. (d) Calibration curve of the sensor showing the response between current and logarithm of cMb.

Fig. 8. (a) DPV response of the microfluidic chip with RGO hydrogel (cMAb/Cys-RGO/Au) in presence of cMb (0.004–1000 ng/mL). (b) calibration plot of the sensor presenting the response current versus logarithm concentration of cMb. (c) DPV response of the cMAb/Cys-RGO/Au sensor for serum cMb (0.04–500 ng/mL). (d) Calibration curve of the sensor presenting the output current versus logarithm of serum cMb concentration. (e) Curves for DPV response current of the sensor answering to lab prepared standard cMb sample and human serums of cMb. The relative standard deviation (%RSD) for all concentrations were determined of three repeated measurements with error bars. (f) Control study using Cys-RGO/Au electrode without incorporating antibody in presence of standard cMb samples (0.2 to 500 ng mL^{-1}) and compared with cMb/Cys-RGO/Au sensor.

Fig. 9. (a) SPR response of the immobilization of cMAb on the Cys-RGO/Au sensor. (b) SPR curve of immobilization of cMAb. (c) SPR sensing response of the cMAb/Cys-RGO/Au sensor as a function of cMb (0.01–1000 ng/mL). (d) Calibration curve of SPR sensor showing the output SPR angle versus logarithm of cMb concentration.

Fig. 10. (a) DPV response of selectivity test of the sensor in presence of 100 ng/mL cMb and with the addition of 100 ng/mL interferents. (b) Histogram plot of selectivity shows the current responses versus various interferents. (c) Reproducibility test of the sensor conducted with four similar sensors at 100 ng/mL of cMb. Inset reveals the histogram plot of the current response versus four identical sensors. (d) Stability test of the sensor was determined for six weeks at 5 ng/mL cMb concentration once a week over a six-week period.

References

1 L. Zhai, *Chem. Soc. Rev.*, 2013, **42**, 7148–7160.
2 H. S. Song, O. S. Kwon, J.-H. Kim, J. Conde and N. Artzi, *Biosens. Bioelectron.*, 2017, **89**, 187–200.
3 Y. Cheng, K. Ren, C. Huang and J. Wei, *Sens. Actuators B Chem.*, 2019, **298**, 126908.
4 C. Huang, Y. Cheng, Z. Gao, H. Zhang and J. Wei, *Sens. Actuators B Chem.*, 2018, **273**, 1705–1712.
5 S. L. Burrs, D. C. Vanegas, M. Bhargava, N. Mechulan, P. Hendershot, H. Yamaguchi, C. Gomes and E. S. McLamore, *Analyst*, 2015, **140**, 1466–1476.
6 K. Kostarelos and K. S. Novoselov, *Science*, 2014, **344**, 261–263.
7 O. Ö. Ekiz, M. Ürel, H. Güner, A. K. Mizrak and A. Dâna, *ACS Nano*, 2011, **5**, 2475–2482.
8 Y. Shao, J. Wang, H. Wu, J. Liu, I. A. Aksay and Y. Lin, *Electroanalysis*, 2010, **22**, 1027–1036.
9 S. Cui, H. Pu, E. C. Mattson, Z. Wen, J. Chang, Y. Hou, C. J. Hirschmugl and J. Chen, *Anal. Chem.*, 2014, **86**, 7516–7522.
10 M. Pumera, A. Ambrosi, A. Bonanni, E. L. K. Chng and H. L. Poh, *TrAC Trends Anal. Chem.*, 2010, **29**, 954–965.
11 R. Singh, S. Hong and J. Jang, *Sci. Rep.*, 2017, **7**, 42771.
12 Y. Wu, P. Xue, Y. Kang and K. M. Hui, *Anal. Chem.*, 2013, **85**, 8661–8668.
13 P. Batalla, A. Martín, M. Á. López, M. C. González and A. Escarpa, *Anal. Chem.*, 2015, **87**, 5074–5078.

View Article Online
DOI: 10.1039/C9LC00751B

14 J. Kim, S.-J. Park and D.-H. Min, *Anal. Chem.*, 2017, **89**, 232–248.
15 A. Bagri, C. Mattevi, M. Acik, Y. J. Chabal, M. Chhowalla and V. B. Shenoy, *Nat. Chem.*, 2010, **2**, 581–587.
16 Y. Wang, Y. Xiao, G. Gao, J. Chen, R. Hou, Q. Wang, L. Liu and J. Fu, *J. Mater. Chem. B*, 2017, **5**, 511–516.
17 Md. A. Ali, S. Srivastava, M. K. Pandey, V. V. Agrawal, R. John and B. D. Malhotra, *Anal. Chem.*, 2014, **86**, 1710–1718.
18 J. Zhang, S. Yan, D. Yuan, G. Alici, N.-T. Nguyen, M. E. Warkiani and W. Li, *Lab. Chip*, 2016, **16**, 10–34.
19 E. K. Sackmann, A. L. Fulton and D. J. Beebe, *Nature*, 2014, **507**, 181–189.
20 B. Zribi, E. Roy, A. Pallandre, S. Chebil, M. Koubaa, N. Mejri, H. Magdinier Gomez, C. Sola, H. Korri-Youssoufi and A.-M. Haghiri-Gosnet, *Biomicrofluidics*, 2016, **10**, 014115.
21 N. Singh, Md. A. Ali, P. Rai, A. Sharma, B. D. Malhotra and R. John, *ACS Appl. Mater. Interfaces*, 2017, **9**, 33576–33588.
22 N. Wongkaew, M. Simsek, C. Griesche and A. J. Baeumner, *Chem. Rev.*, 2019, **119**, 120–194.
23 L. Reverté, B. Prieto-Simón and M. Campàs, *Anal. Chim. Acta*, 2016, **908**, 8–21.
24 C. Zhu, G. Yang, H. Li, D. Du and Y. Lin, *Anal. Chem.*, 2015, **87**, 230–249.
25 G. K. Mani, M. Morohoshi, Y. Yasoda, S. Yokoyama, H. Kimura and K. Tsuchiya, *ACS Appl. Mater. Interfaces*, 2017, **9**, 5193–5203.
26 M. Medina-Sánchez, C. C. Mayorga-Martinez, T. Watanabe, T. A. Ivandini, Y. Honda, F. Pino, K. Nakata, A. Fujishima, Y. Einaga and A. Merkoçi, *Biosens. Bioelectron.*, 2016, **75**, 365–374.
27 N. Singh, P. Rai, M. Azahar Ali, R. Kumar, A. Sharma, B. D. Malhotra and R. John, *J. Mater. Chem. B*, 2019, **7**, 3826–3839.
28 X. Li, C. Zhao and X. Liu, *Microsyst. Nanoeng.*, 2015, **1**, 15014.
29 M. Azahar Ali, S. Tabassum, Q. Wang, Y. Wang, R. Kumar and L. Dong, *Lab. Chip*, 2018, **18**, 803–817.
30 M. Singh, M. Holzinger, M. Tabrizian, S. Winters, N. C. Berner, S. Cosnier and G. S. Duesberg, *J. Am. Chem. Soc.*, 2015, **137**, 2800–2803.
31 E. N. Primo, M. J. Kogan, H. E. Verdejo, S. Bollo, M. D. Rubianes and G. A. Rivas, *ACS Appl. Mater. Interfaces*, 2018, **10**, 23501–23508.
32 A. Qureshi, Y. Gurbuz and J. H. Niazi, *Sens. Actuators B Chem.*, 2012, **171–172**, 62–76.
33 D. Sharma, J. Lee and H. Shin, *Biosens. Bioelectron.*, 2018, **107**, 10–16.
34 N. K. Bakirhan, G. Ozcelikay and S. A. Ozkan, *J. Pharm. Biomed. Anal.*, 2018, **159**, 406–424.
35 J. Salas-Salvadó, N. Becerra-Tomás, J. F. García-Gavilán, M. Bulló and L. Barrubés, *Prog. Cardiovasc. Dis.*, 2018, **61**, 62–67.
36 A. M. Piloto, D. S. M. Ribeiro, S. S. M. Rodrigues, C. Santos, J. L. M. Santos and M. G. F. Sales, *Sci. Rep.*, 2018, **8**, 4944.
37 F. S. Apple, A. Falahati, P. R. Paulsen, E. A. Miller and S. W. Sharkey, *Clin. Chem.*, 1997, **43**, 2047–2051.
38 C. A. Marquette, F. Bouteille, B. P. Corgier, A. Degiuli and L. J. Blum, *Anal. Bioanal. Chem.*, 2009, **393**, 1191–1198.
39 I.-H. Cho, E.-H. Paek, Y.-K. Kim, J.-H. Kim and S.-H. Paek, *Anal. Chim. Acta*, 2009, **632**, 247–255.
40 J. Wang, A. Ibáñez, M. P. Chatrathi and A. Escarpa, *Anal. Chem.*, 2001, **73**, 5323–5327.
41 M.-I. Mohammed and M. P. Y. Desmulliez, *Lab. Chip*, 2011, **11**, 569–595.
42 Md. A. Ali, K. Kamil Reza, S. Srivastava, V. V. Agrawal, R. John and B. D. Malhotra, *Langmuir*, 2014, **30**, 4192–4201.
43 A. J. Bard, L. R. Faulkner, J. Leddy and C. G. Zoski, *Electrochemical methods: fundamentals and applications*, wiley New York, 1980, vol. 2.
44 J. Wang, *Analytical electrochemistry*, Wiley-VCH, Hoboken, NJ, 2006.
45 J. Homola, S. S. Yee and G. Gauglitz, *Sens. Actuators B Chem.*, 1999, **54**, 3–15.
46 H. H. Nguyen, J. Park, S. Kang and M. Kim, *Sensors*, 2015, **15**, 10481–10510.
47 G. Williams, B. Seger and P. V. Kamat, *ACS Nano*, 2008, **2**, 1487–1491.

View Article Online
DOI: 10.1039/C9LC00751B

48 P. Bazylewski, R. Divigalpitiya and G. Fanchini, *RSC Adv.*, 2017, **7**, 2964–2970.
49 S. Srivastava, V. Kumar, M. Azahar Ali, P. R. Solanki, A. Srivastava, G. Sumana, P. Suman Saxena, A. G. Joshi and B. D. Malhotra, *Nanoscale*, 2013, **5**, 3043–3051.
50 K. C. Nguyen, *Adv. Nat. Sci. Nanosci. Nanotechnol.*, 2012, **3**, 045008.
51 A. S. K. Kumar and S.-J. Jiang, *RSC Adv.*, 2015, **5**, 6294–6304.
52 D. B. Mawhinney, V. Naumenko, A. Kuznetsova, J. T. Yates, J. Liu and R. E. Smalley, *J. Am. Chem. Soc.*, 2000, **122**, 2383–2384.
53 T. Ramanathan, F. T. Fisher, R. S. Ruoff and L. C. Brinson, *Chem. Mater.*, 2005, **17**, 1290–1295.
54 S. Aryal, R. B.k.c., N. Dharmaraj, N. Bhattarai, C. H. Kim and H. Y. Kim, *Spectrochim. Acta. A. Mol. Biomol. Spectrosc.*, 2006, **63**, 160–163.
55 X. Gong, Y. Bi, Y. Zhao, G. Liu and W. Yang Teoh, *RSC Adv.*, 2014, **4**, 24653–24657.
56 W. Liu, D. Sun, J. Fu, R. Yuan and Z. Li, *RSC Adv.*, 2014, **4**, 11003–11011.
57 N. Tawil, E. Sacher, E. Boulais, R. Mandeville and M. Meunier, *J. Phys. Chem. C*, 2013, **117**, 20656–20665.
58 O. V. Gnedenko, Y. V. Mezentsev, A. A. Molnar, A. V. Lisitsa, A. S. Ivanov and A. I. Archakov, *Anal. Chim. Acta*, 2013, **759**, 105–109.
59 V. Kumar, M. Shorie, A. K. Ganguli and P. Sabherwal, *Biosens. Bioelectron.*, 2015, **72**, 56–60.
60 Rajesh, V. Sharma, V. K. Tanwar, S. K. Mishra and A. M. Biradar, *Thin Solid Films*, 2010, **519**, 1167–1170.
61 S. Singh, S. K. Tuteja, D. Sillu, A. Deep and C. R. Suri, *Microchim. Acta*, 2016, **183**, 1729–1738.
62 S. K. Tuteja, R. Chen, M. Kukkar, C. K. Song, R. Mutreja, S. Singh, A. K. Paul, H. Lee, K.-H. Kim, A. Deep and C. R. Suri, *Biosens. Bioelectron.*, 2016, **86**, 548–556.
63 S. M. Taghdisi, N. M. Danesh, M. Ramezani, A. S. Emrani and K. Abnous, *Biosens. Bioelectron.*, 2016, **80**, 532–537.
64 L. Sun, W. Li, M. Wang, W. Ding and Y. Ji, *Int J Electrochem Sci*, 2017, **12**, 6170–6179.
65 M. Adeel, Md. M. Rahman and J.-J. Lee, *Biosens. Bioelectron.*, 2019, **126**, 143–150.
66 R. Khan, M. Pal, A. V. Kuzikov, T. Bulko, E. V. Suprun and V. V. Shumyantseva, *Mater. Sci. Eng. C*, 2016, **68**, 52–58.

View Article Online
DOI: 10.1039/C9LC00751B

Figures

Fig.1

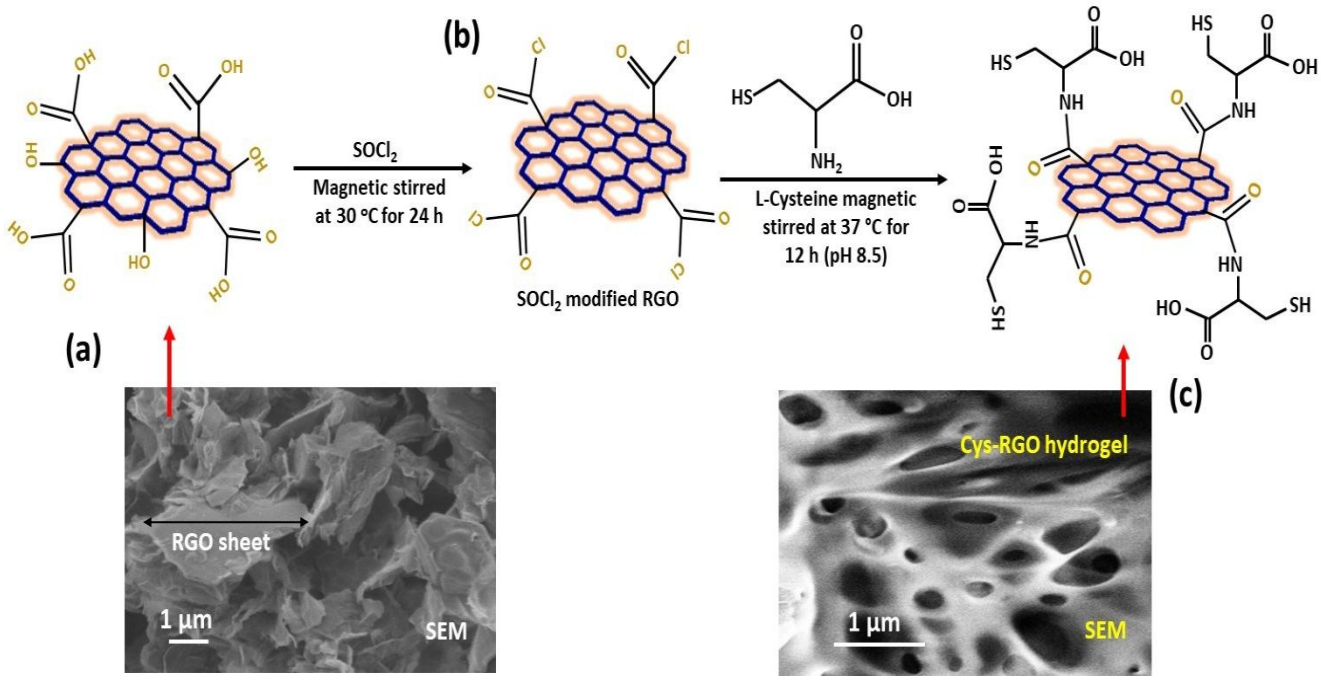

View Article Online
DOI: 10.1039/C9LC00751B

Fig.2

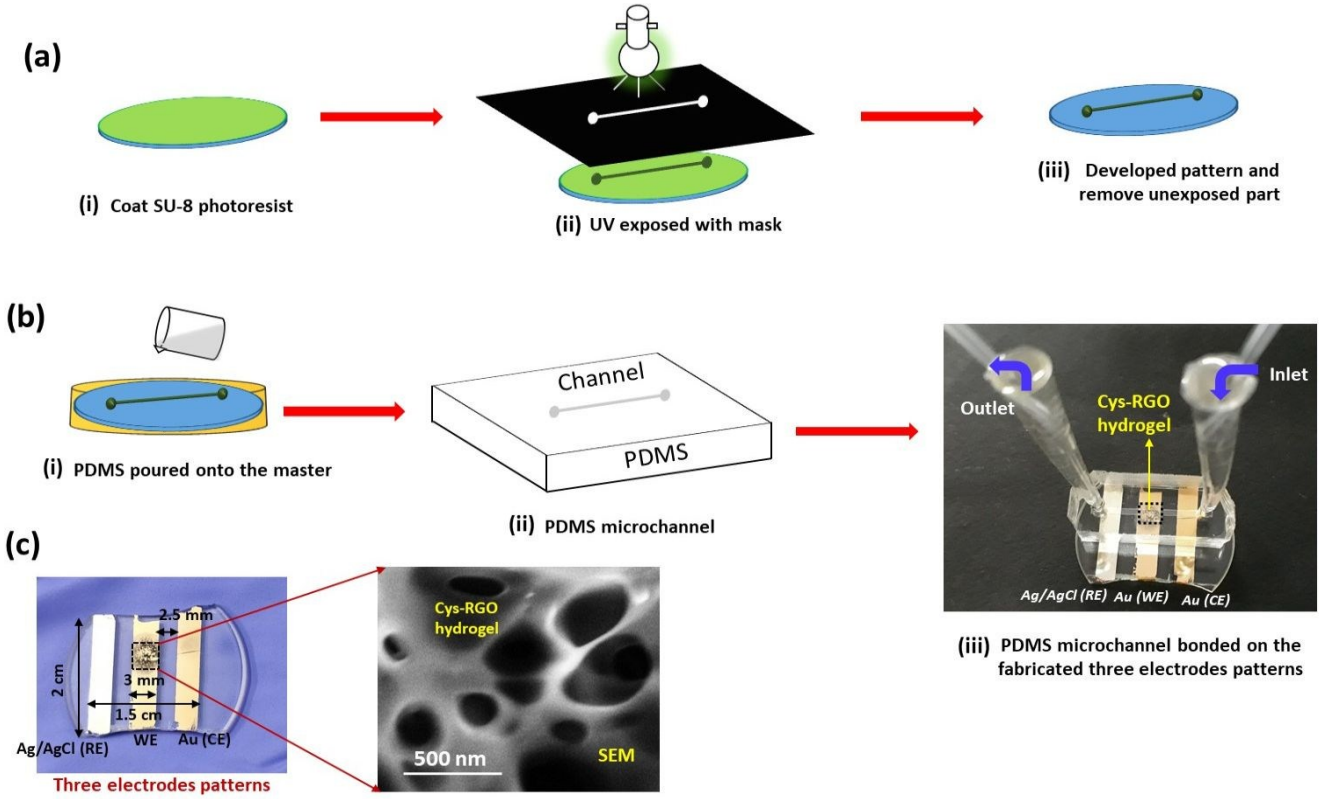

View Article Online
DOI: 10.1039/C9LC00751B

Fig.3

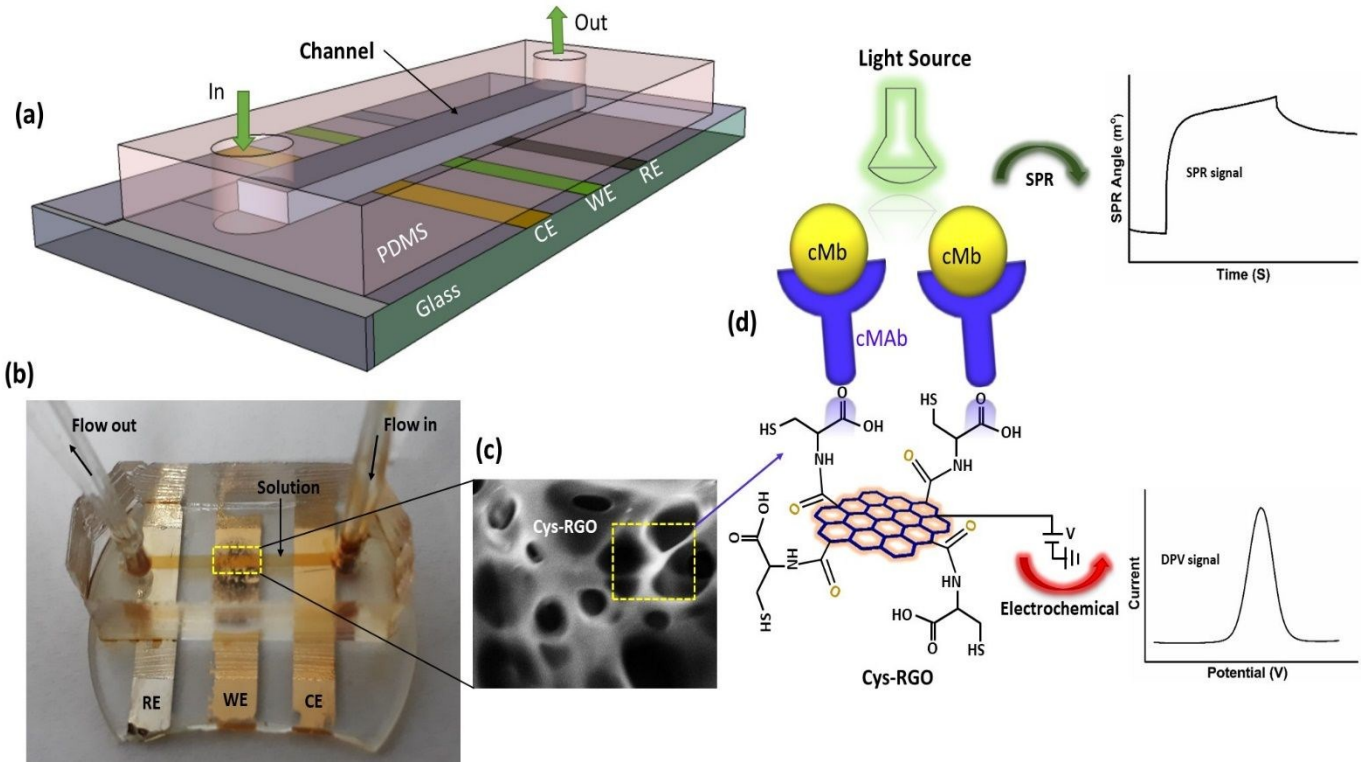

View Article Online
DOI: 10.1039/C9LC00751B

Fig.4

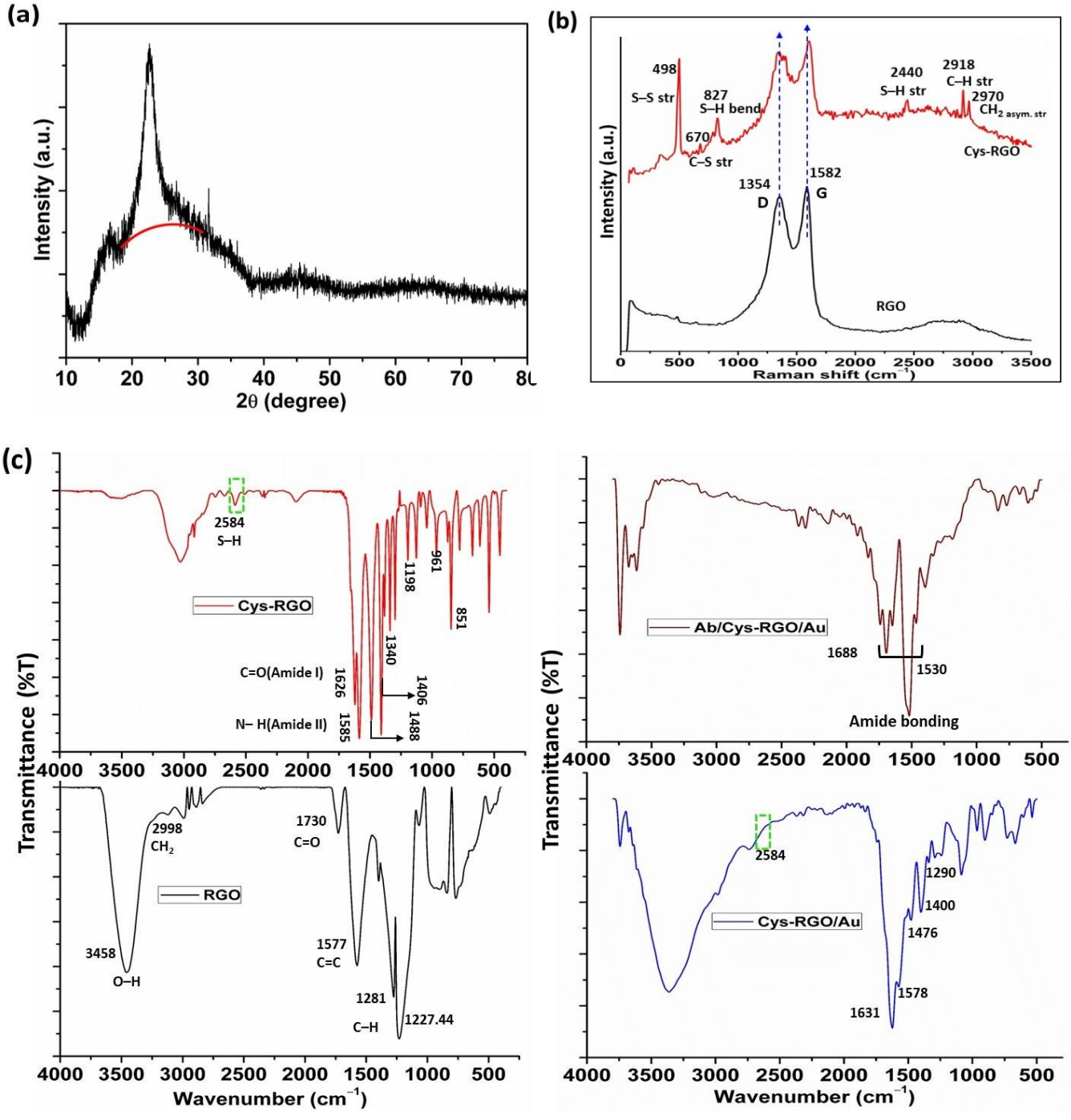

Fig.5

View Article Online
DOI: 10.1039/C9LC00751B

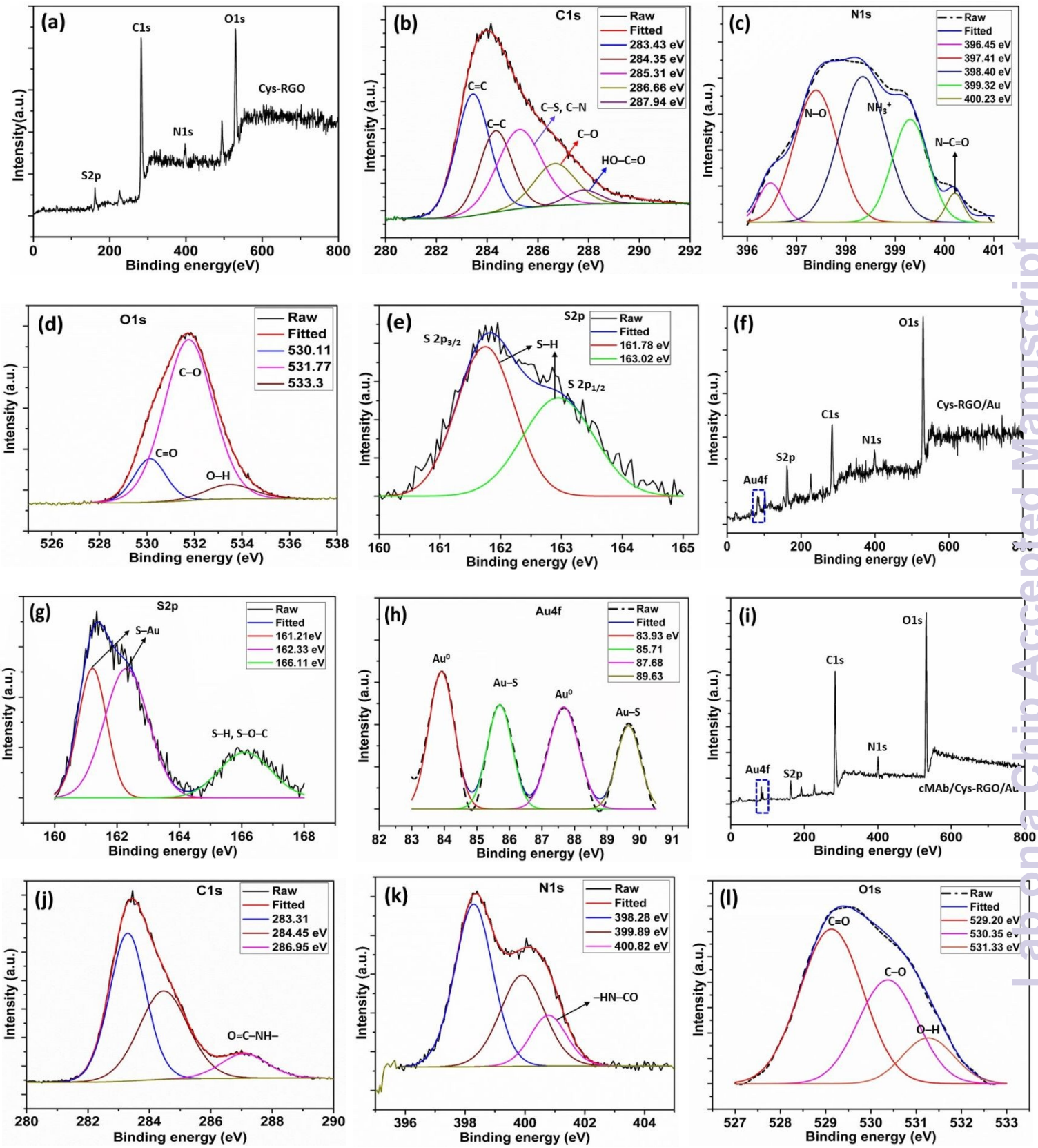

Fig.6

View Article Online
DOI: 10.1039/C9LC00751B

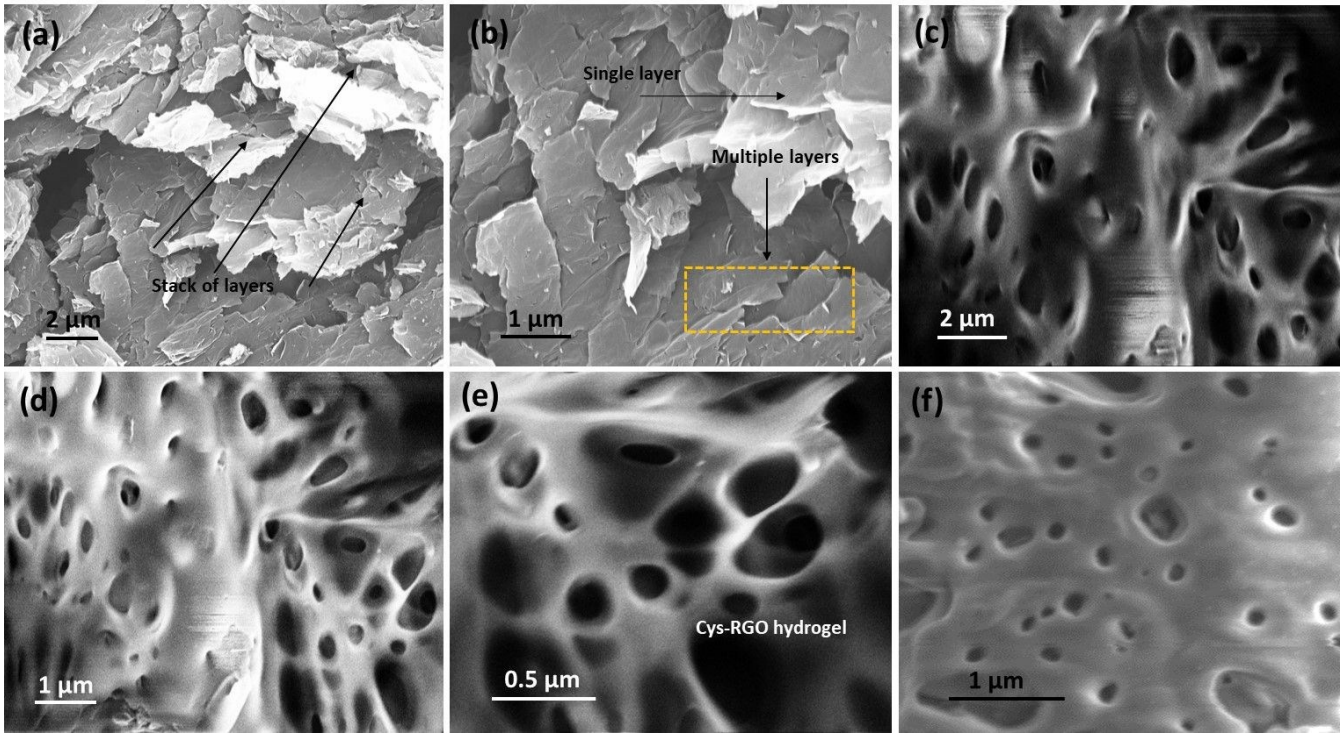

View Article Online
DOI: 10.1039/C9LC00751B

Fig.7

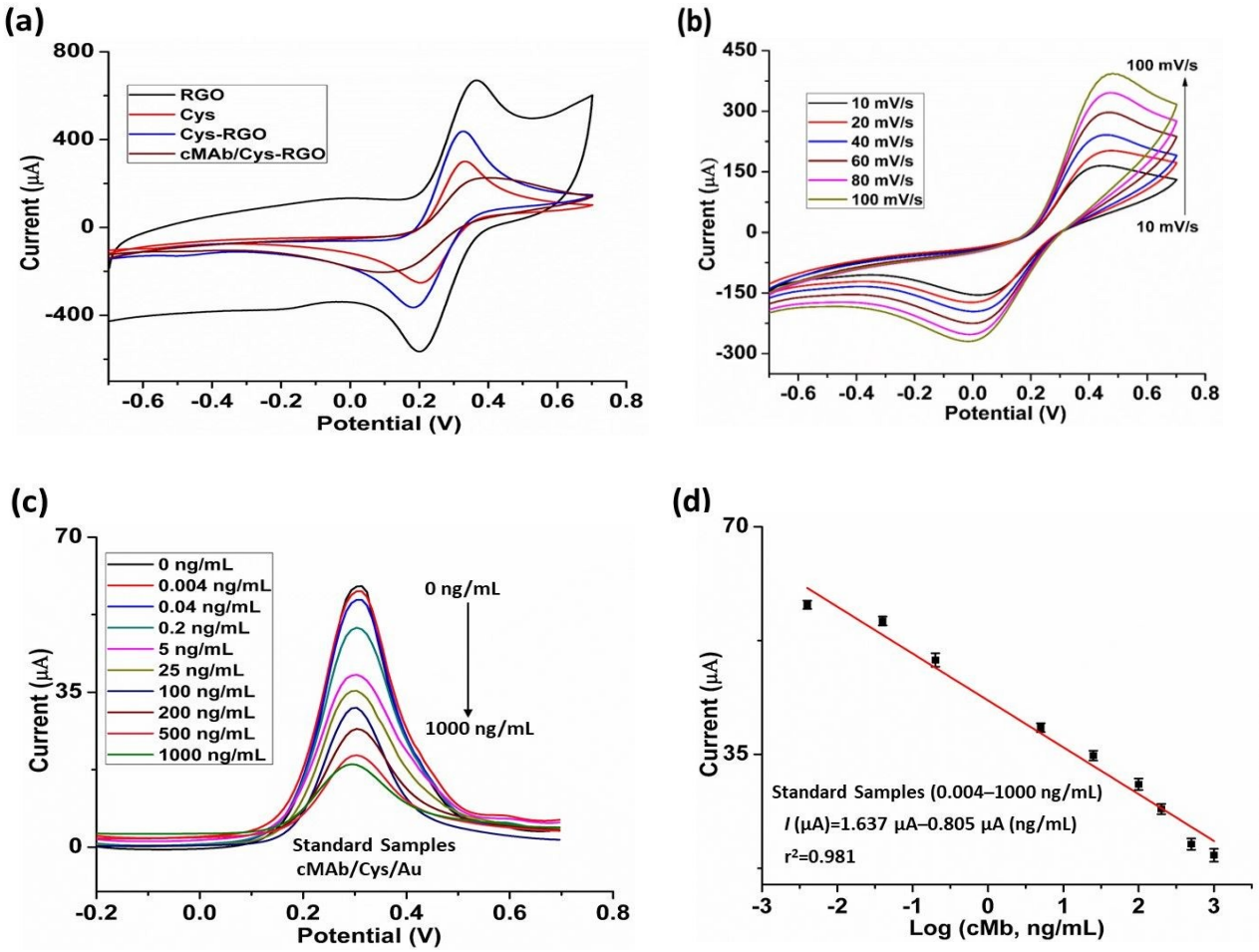

View Article Online
DOI: 10.1039/C9LC00751B

Fig.8

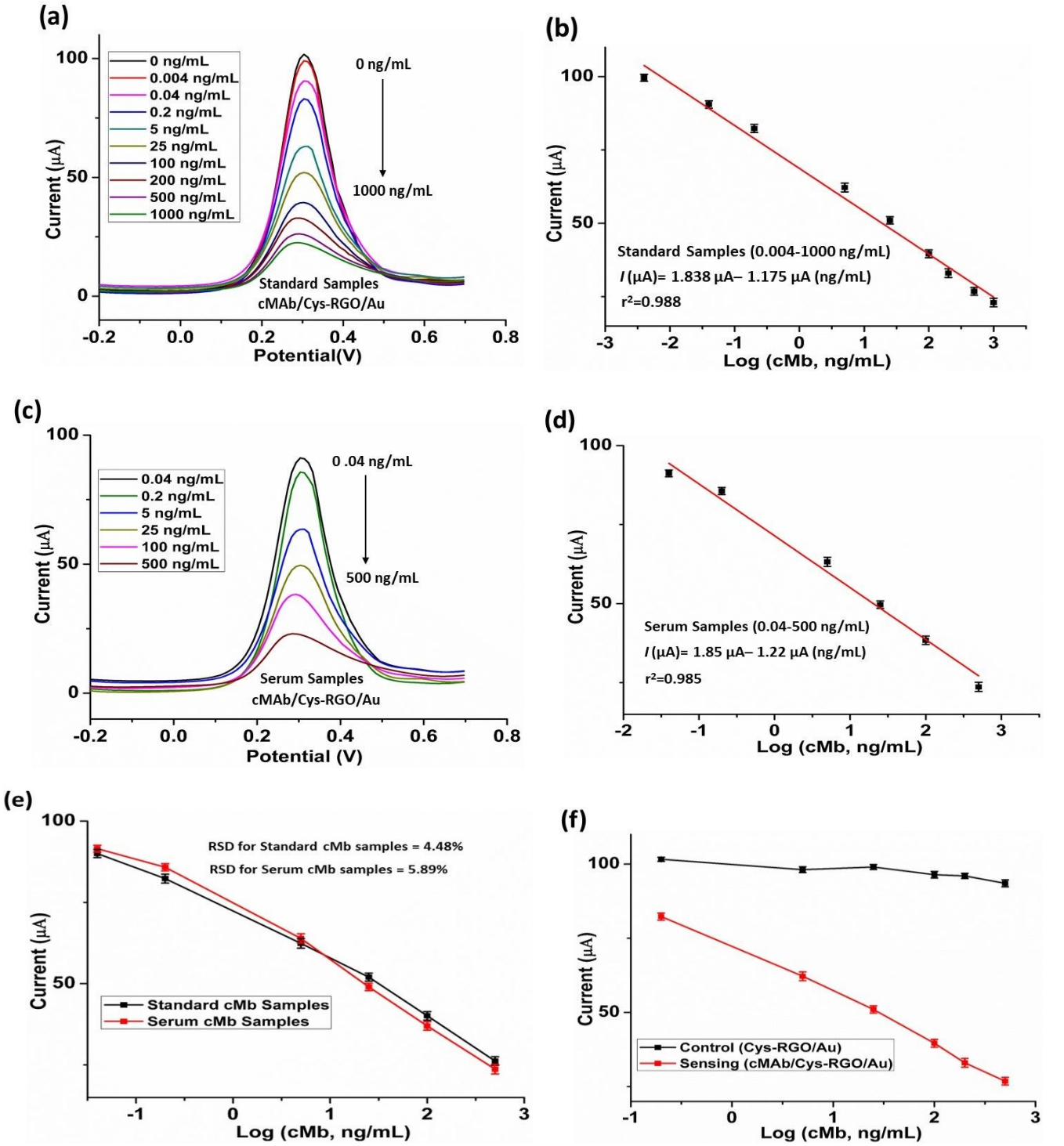

Fig.9

View Article Online
DOI: 10.1039/C9LC00751B

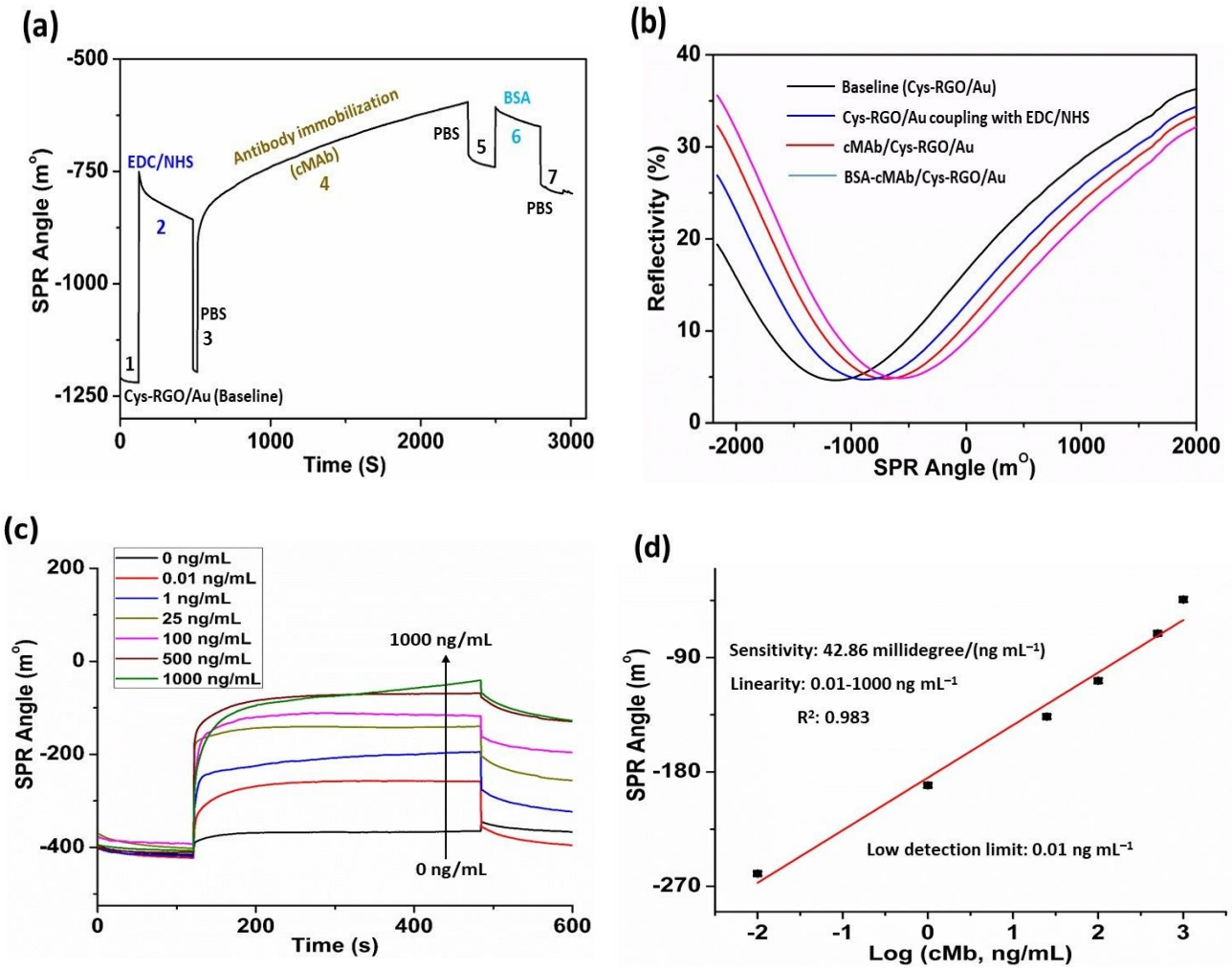

Fig.10

View Article Online
DOI: 10.1039/C9LC00751B

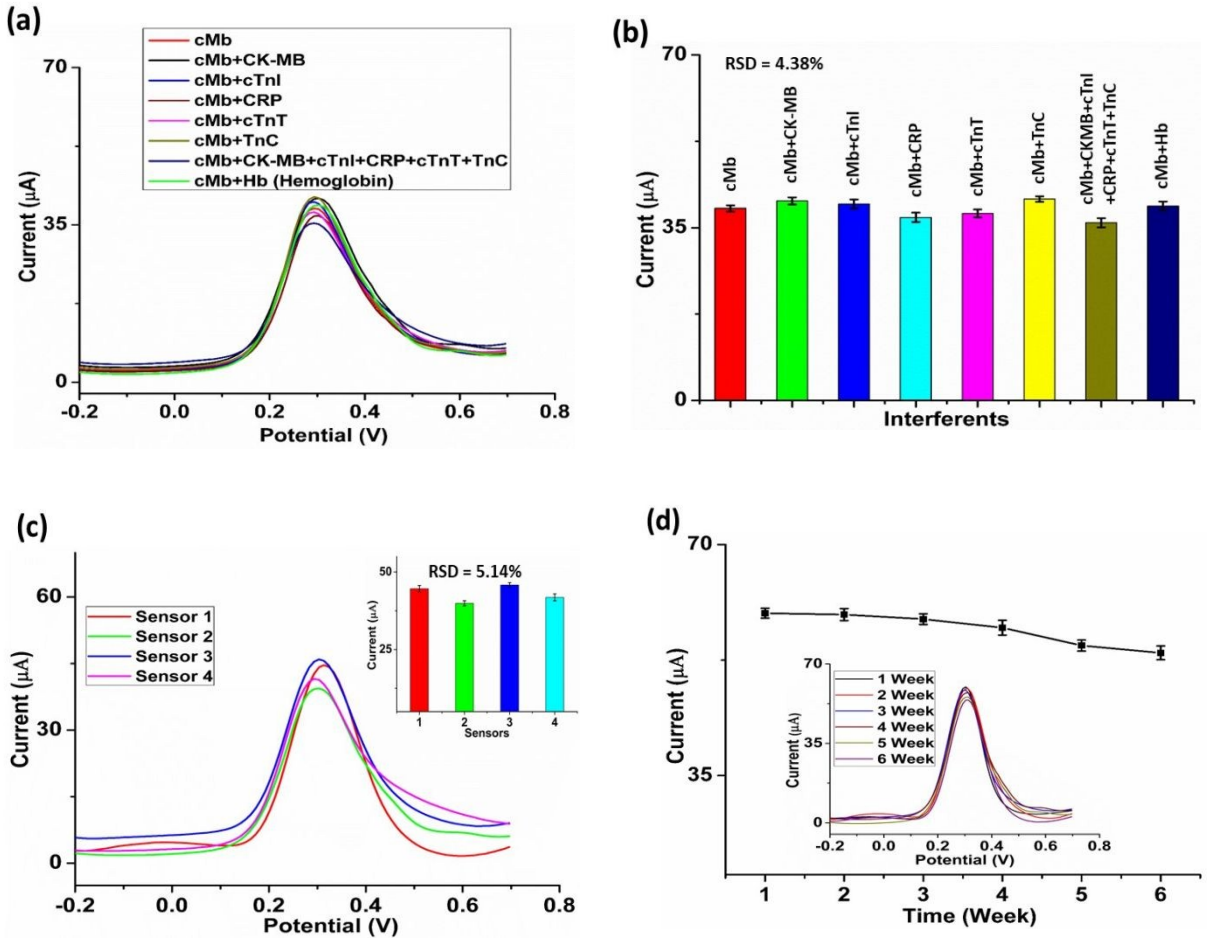

View Article Online
DOI: 10.1039/C9LC00751B

Graphical abstract